Prepared for submission to JHEP

Measurements of the mass difference $m(B^0) - m(B^+)$ and the energy dependence of the cross-section ratio $\sigma(e^+e^- \to B^0\bar{B}^0) \,/\, \sigma(e^+e^- \to B^+B^-)$ at Belle and Belle II

The Belle and Belle II Collaborations

M. Abumusabh, I. Adachi, L. Aggarwal, H. Ahmed, Y. Ahn, H. Aihara, N. Akopov, S. Alghamdi, M. Alhakami, A. Aloisio, N. Althubiti, K. Amos, N. Anh Ky, C. Antonioli, D. M. Asner, H. Atmacan, T. Aushev, R. Ayad, V. Babu, N. K. Baghel, S. Bahinipati, P. Bambade, Sw. Banerjee, M. Barrett, M. Bartl, J. Baudot, A. Beaubien, F. Becherer, J. Becker, J. V. Bennett, F. U. Bernlochner, V. Bertacchi, M. Bertemes, E. Bertholet, M. Bessner, S. Bettarini, V. Bhardwaj, F. Bianchi, T. Bilka, D. Biswas, D. Bodrov, A. Bondar, G. Bonvicini, J. Borah, A. Boschetti, A. Bozek, M. Bračko, P. Branchini, R. A. Briere, T. E. Browder, A. Budano, S. Bussino, Q. Campagna, M. Campajola, G. Casarosa, C. Cecchi, P. Chang, P. Cheema, L. Chen, B. G. Cheon, C. Cheshta, H. Chetri, K. Chilikin, J. Chin, K. Chirapatpimol, H.-E. Cho, K. Cho, S.-J. Cho, S.-K. Choi, S. Choudhury, S. Chutia, J. A. Colorado-Caicedo, I. Consigny, L. Corona, J. X. Cui, E. De La Cruz-Burelo, S. A. De La Motte, G. de Marino, G. De Nardo, G. De Pietro, R. de Sangro, M. Destefanis, S. Dey, A. Di Canto, Z. Doležal, I. Domínguez Jiménez, T. V. Dong, X. Dong, M. Dorigo, G. Dujany, P. Ecker, J. Eppelt, R. Farkas, P. Feichtinger, T. Ferber, T. Fillinger, C. Finck, G. Finocchiaro, F. Forti, B. G. Fulsom, A. Gabrielli, A. Gale, E. Ganiev, M. Garcia-Hernandez, R. Garg, G. Gaudino, V. Gaur, V. Gautam, A. Gaz, A. Gellrich, G. Ghevondyan, D. Ghosh, H. Ghumaryan, G. Giakoustidis, R. Giordano, A. Giri, P. Gironella Gironell, A. Glazov, B. Gobbo, R. Godang, O. Gogota, P. Goldenzweig, W. Gradl, E. Graziani, D. Greenwald, K. Gudkova, I. Haide, Y. Han, H. Hayashii, S. Hazra, C. Hearty, M. T. Hedges, A. Heidelbach, I. Heredia de la Cruz, M. Hernández Villanueva, T. Higuchi, M. Hoek, M. Hohmann, R. Hoppe, P. Horak, X. T. Hou, C.-L. Hsu, T. Humair, T. Iijima, N. Ipsita, A. Ishikawa, R. Itoh, M. Iwasaki, D. Jacobi, W. W. Jacobs, D. E. Jaffe, E.-J. Jang, Q. P. Ji, S. Jia,

Y. Jin, A. Johnson, A. B. Kaliyar, J. Kandra, K. H. Kang, S. Kang, G. Karyan, F. Keil, C. Kiesling, D. Y. Kim, J.-Y. Kim, K.-H. Kim, H. Kindo, K. Kinoshita, P. Kodyš, T. Koga, S. Kohani, K. Kojima, A. Korobov, S. Korpar, R. Kowalewski, P. Križan, P. Krokovny, T. Kuhr, D. Kumar, K. Kumara, T. Kunigo, A. Kuzmin, Y.-J. Kwon, S. Lacaprara, T. Lam, L. Lanceri, J. S. Lange, T. S. Lau, M. Laurenza, R. Leboucher, F. R. Le Diberder, H. Lee, M. J. Lee, C. Lemettais, P. Leo, P. M. Lewis, C. Li, H.-J. Li, L. K. Li, Q. M. Li, W. Z. Li, Y. Li, Y. B. Li, Y. P. Liao, J. Libby, J. Lin, S. Lin, V. Lisovskyi, M. H. Liu, Q. Y. Liu, D. Liventsev, S. Longo, A. Lozar, T. Lueck, C. Lyu, J. L. Ma, Y. Ma, M. Maggiora, S. P. Maharana, R. Maiti, G. Mancinelli, R. Manfredi, E. Manoni, M. Mantovano, D. Marcantonio, M. Marfoli, C. Marinas, C. Martellini, A. Martens, T. Martinov, L. Massaccesi, M. Masuda, D. Matvienko, S. K. Maurya, M. Maushart, J. A. McKenna, Z. Mediankin Gruberová, R. Mehta, F. Meier, D. Meleshko, M. Merola, C. Miller, M. Mirra, K. Miyabayashi, H. Miyake, R. Mizuk, G. B. Mohanty, S. Moneta, A. L. Moreira de Carvalho, H.-G. Moser, M. Mrvar, H. Murakami, I. Nakamura, M. Nakao, Y. Nakazawa, M. Naruki, Z. Natkaniec, A. Natochii, M. Nayak, M. Neu, S. Nishida, R. Nomaru, S. Ogawa, R. Okubo, H. Ono, F. Otani, G. Pakhlova, A. Panta, S. Pardi, K. Parham, J. Park, S.-H. Park, A. Passeri, S. Patra, S. Paul, T. K. Pedlar, R. Pestotnik, M. Piccolo, L. E. Piilonen, P. L. M. Podesta-Lerma, T. Podobnik, C. Praz, S. Prell, E. Prencipe, M. T. Prim, S. Privalov, H. Purwar, P. Rados, S. Raiz, K. Ravindran, J. U. Rehman, M. Reif, S. Reiter, L. Reuter, D. Ricalde Herrmann, I. Ripp-Baudot, G. Rizzo, S. H. Robertson, J. M. Roney, A. Rostomyan, N. Rout, S. Saha, Y. Sakai, L. Salutari, D. A. Sanders, S. Sandilya, L. Santelj, C. Santos, V. Savinov, B. Scavino, C. Schmitt, S. Schneider, G. Schnell, M. Schnepf, K. Schoenning, C. Schwanda, Y. Seino, K. Senyo, J. Serrano, M. E. Sevior, C. Sfienti, W. Shan, G. Sharma, X. D. Shi, T. Shillington, J.-G. Shiu, D. Shtol, B. Shwartz, A. Sibidanov, F. Simon, J. Skorupa, R. J. Sobie, M. Sobotzik, A. Soffer, A. Sokolov, E. Solovieva, S. Spataro, K. Špenko, B. Spruck, M. Starič, P. Stavroulakis, R. Stroili, M. Sumihama, M. Takahashi, U. Tamponi, S. S. Tang, K. Tanida, F. Tenchini, F. Testa, A. Thaller, T. Tien Manh, O. Tittel, R. Tiwary, E. Torassa, K. Trabelsi, F. F. Trantou, I. Ueda, K. Unger, Y. Unno, K. Uno, S. Uno, P. Urquijo, Y. Ushiroda, S. E. Vahsen, R. van Tonder, K. E. Varvell, M. Veronesi, V. S. Vismaya, L. Vitale, V. Vobbilisetti, R. Volpe, M. Wakai, S. Wallner, M.-Z. Wang, A. Warburton, M. Watanabe, S. Watanuki, C. Wessel, E. Won, X. P. Xu, B. D. Yabsley, W. Yan, W. Yan, J. Yelton, K. Yi, J. H. Yin, K. Yoshihara, J. Yuan, L. Zani, F. Zeng, M. Zeyrek, B. Zhang, V. Zhilich, J. S. Zhou, Q. D. Zhou, L. Zhu, R. Žlebčík

Abstract: Using data samples collected by the Belle and Belle II experiments at the $\Upsilon(4S)$ resonance with integrated luminosities of $571\,\mathrm{fb}^{-1}$ and $365\,\mathrm{fb}^{-1}$, respectively, we measure the pseudoscalar B-meson mass difference to be $m(B^0)-m(B^+) = (0.495\pm0.024\pm 0.005)\,\mathrm{MeV}/c^2$. The results are based on a simultaneous fit to the variable $\tilde{M}_{\mathrm{bc}}$, which is related to the B momentum, for B^0 and B^+ candidates; and to the energy dependence of $\mathcal{R} = \sigma(e^+e^- \to B^0\bar{B}^0)\,/\,\sigma(e^+e^- \to B^+B^-)$, which is measured using changes in the average center-of-mass energy over the data taking periods. The phase-space hypothesis $\mathcal{R} = (p_{B^0}/p_{B^+})^3$, upon which previous measurements rely, is strongly disfavored by our fit; the measured mass-difference value for the phase-space hypothesis also differs significantly from our measurement. We constrain $\mathcal{R}$ in a broader energy range than covered by the direct measurement and extract the energy dependence of $\mathcal{R}$ in the range from the $B\bar{B}$ threshold up to $10.59\,\mathrm{GeV}$. We interpret the results using a phenomenological model and constrain the parameters of the $B\bar{B}$ potential in the isovector channel.

Keywords: B Physics, e^+e^- Experiments, Quarkonium, Spectroscopy

Contents

1 Introduction

The mass difference between the B^0 and B^+ mesons, $\Delta m = m(B^0) - m(B^+)$, is an isospin-violating effect that arises due to the mass difference between the u and d quarks and the electromagnetic interaction between the b quark and the light antiquarks. The value of Δm is sensitive to the masses of the u and d quarks and provides a constraint on the B-meson wave function [1]. The energy dependence of the cross-section ratio $\sigma(e^+e^- \to B^0\bar{B}^0)\,/\,\sigma(e^+e^- \to B^+B^-)$ near the meson pair mass threshold provides information about the $B\bar{B}$ potential in the isovector channel [2], which is important for understanding $B^{(*)}\bar{B}^{(*)}$ molecular states with isospin one [3].

We measure Δm using differences in the momentum distributions of neutral and charged B-meson pairs produced at the $\Upsilon(4S)$ resonance. The momentum distributions of B^0 and B^+ are different for the following two reasons:

(a) The masses of B^0 and B^+ are different; this is the source of the sensitivity of our method.

(b) The energy distributions of B^0 and B^+ are different due to the finite spread of the e^+e^- collision energy in the center-of-mass (c.m.) system, $E_{\rm cm}$, and the different energy dependences of the $e^+e^- \to B^0\bar{B}^0$ and $e^+e^- \to B^+B^-$ cross sections.

For a precise measurement of Δm, it is essential to take correctly into account the effect of (b), for which the energy dependence of the cross-section ratio

$$\mathcal{R} = \frac{\sigma(e^+e^- \to B^0\bar{B}^0)}{\sigma(e^+e^- \to B^+B^-)} \tag{1.1}$$

is required [4]. However, the dependence $\mathcal{R}(E_{\rm cm})$ has not been measured and there are no reliable theoretical predictions for it [2, 5, 6]. Our strategy is to measure both Δm and $\mathcal{R}(E_{\rm cm})$ in this analysis; to obtain $\mathcal{R}(E_{\rm cm})$ we use the variations of average $E_{\rm cm}$ over the Belle and Belle II running periods. We use data from the Belle and Belle II experiments collected near the $\Upsilon(4S)$ with integrated luminosities of 571 fb^{-1} and 365 fb^{-1}, respectively. (A 47 fb^{-1} sample of Belle II data taken below the resonance, at 10.52 GeV, is used to make an auxiliary measurement: see section 7.)

The current world-average of Δm is dominated by the BaBar measurement, $\Delta m = (0.33 \pm 0.05 \pm 0.03)\,\text{MeV}/c^2$ [7], which was determined using the average c.m. momenta of B^0 and B^+ mesons produced at the $\Upsilon(4S)$ resonance. For the energy dependence of $\mathcal{R}$ it was assumed that

$$\mathcal{R} = (p_{B^0}/p_{B^+})^3\,. \tag{1.2}$$

This assumption is not justified [2, 5, 6]; in ref. [4] it was pointed out that the change of $\mathcal{R}$ with energy could be much faster than the expectation from eq. (1.2), which could lead to a bias in the Δm measurement by as much as $0.4\,\text{MeV}/c^2$.[1] Thus, it is important to measure the energy dependence of $\mathcal{R}$.

To fully exploit the available information for the measurement of Δm and $\mathcal{R}(E_{\rm cm})$, we develop a combined fit to several distributions that are sensitive to the quantities of interest. They are the following (the details of each are described below in sections 4, 5, 6, and 7):

- The $\tilde{M}_{\rm bc}$ distributions of B^0 and B^+ candidates at Belle and Belle II. The $\tilde{M}_{\rm bc}$ variable is uniquely related to the B momentum,

$$\tilde{M}_{\rm bc} = \sqrt{\left(\frac{m_{\Upsilon(4S)}}{2}\right)^2 - p_B^2}, \tag{1.3}$$

[1] The RMS of the $E_{\rm cm}$ spread is about 5 MeV, which corresponds to a FWHM of 12 MeV. This is only a factor of 0.6 lower than the width of the $\Upsilon(4S)$. Thus, the energy interval spanned by the $E_{\rm cm}$ spread is large, which explains why the effect of the $\mathcal{R}(E_{\rm cm})$ shape on the Δm measurement is so significant.

where $m_{\Upsilon(4S)} = 10.58\,\mathrm{GeV}/c^2$ is approximately the known $\Upsilon(4S)$ mass [8] and B denotes B^0 or B^+. The $\tilde{M}_{\rm bc}$ variable is more convenient than the momentum because the shape of the combinatorial background near the kinematic boundary $p_B = 0$ is simpler.

The $\tilde{M}_{\rm bc}$ distribution for B^0 (B^+) depends on the $E_{\rm cm}$ distribution, the line-shape of the $B^0\bar{B}^0$ (B^+B^-) cross section, the B^0 (B^+) mass, and the momentum resolution of B^0 (B^+) [9, 10].

- The energy dependence of $\mathcal{R}$ measured using variations in $E_{\rm cm}$ over time. We measure the ratio of the B^0 and B^+ yields in slices of $E_{\rm cm}$, which corresponds to $\mathcal{R}(E_{\rm cm})$.
- The results of an energy scan for $\sigma(e^+e^- \to b\bar{b})$ obtained by the BaBar experiment [11]. Below the $B\bar{B}^*$ threshold, $\sigma(e^+e^- \to b\bar{b}) = \sigma(e^+e^- \to B^0\bar{B}^0) + \sigma(e^+e^- \to B^+B^-)$; the sum of the cross sections, together with $\mathcal{R}(E_{\rm cm})$, is needed to obtain the B^0 and B^+ line-shapes separately.
- The cross section $\sigma(e^+e^- \to b\bar{b} \to D^0/\bar{D}^0\,X)$ versus $E_{\rm cm}$. This constrains the energy scale of the $\sigma(e^+e^- \to b\bar{b})$ scan [11].

The $\tilde{M}_{\rm bc}$ variable is similar to the widely used beam-constrained mass

$$M_{\rm bc} = \sqrt{\bar{E}_B^2 - p_B^2}, \tag{1.4}$$

where $\bar{E}_B$ is the average energy of the B meson for a given running period, determined by calibration (section 5). The $M_{\rm bc}$ distributions for B^0 and B^+ candidates peak at the corresponding nominal masses [8]. The resolution in $\tilde{M}_{\rm bc}$ is slightly worse than the resolution in $M_{\rm bc}$ (by a factor of 1.02 for Belle and by a factor of 1.09 for Belle II), since $\tilde{M}_{\rm bc}$ does not take into account the time variations of the average B-meson energy. The variable $\tilde{M}_{\rm bc}$ is preferred since we can more accurately calculate its shape in the fit function.

The combined fit is sensitive to $\mathcal{R}(E_{\rm cm})$ in a wider energy range than is covered by the time variations of the average collision energy, because the $\tilde{M}_{\rm bc}$ distributions contain information about the line-shapes of the $B^0\bar{B}^0$ and B^+B^- cross sections. The effective sensitivity interval is determined by the $E_{\rm cm}$ spread. Therefore, we report results for $\mathcal{R}(E_{\rm cm})$ from the $B\bar{B}$ threshold of 10.56 GeV up to 10.59 GeV. We then perform a phenomenological analysis of the $\mathcal{R}(E_{\rm cm})$ results to constrain parameters of the isovector $B\bar{B}$ potential.

Our work builds on the previous analyses of Belle [9] and Belle II [10]. We use the same samples of B^0 and B^+ mesons reconstructed in many hadronic final states, and we use a $\tilde{M}_{\rm bc}$ fit function that takes into account the c.m. energy spread, the energy dependence of the production cross section, and all other relevant effects. We also use a simultaneous fit to the $\tilde{M}_{\rm bc}$ distribution and measurements of the energy dependence of the production cross section. The novelty of the current analysis is the use of the time variation of $E_{\rm cm}$ for the cross-section measurements. Furthermore, in refs. [9] and [10] the B^0 and B^+ mesons were combined; here we consider them separately.

The paper is organized as follows. A brief description of the Belle and Belle II detectors and simulation is given in section 2. The selection of B^0 and B^+ candidates is summarized

in section 3. The function used to fit the $\tilde{M}_{\rm bc}$ distributions is presented in section 4. Measurement of $\mathcal{R}$ using $E_{\rm cm}$ variations is described in section 5. The fit to the energy dependence of $\sigma(e^+e^- \to b\bar{b})$ and the measurement of $\sigma(e^+e^- \to b\bar{b} \to D^0\,X)$ are presented in sections 6 and 7, respectively. The results of the combined fit are given in section 8. Systematic uncertainties and additional studies are described in section 9. The measurement of $\mathcal{R}$ in a wide energy range and its phenomenological analysis are reported in sections 10 and 11, respectively. Finally, the conclusions are given in section 12.

2 Detectors and simulation

The Belle experiment [12, 13] operated at the KEKB asymmetric-energy e^+e^- collider [14, 15] between 1999 and 2010. KEKB used 8 GeV electrons and 3.5 GeV positrons. The detector consisted of a large-solid-angle spectrometer, which included a double-sided silicon-strip vertex detector, a 50-layer central drift chamber, an array of aerogel threshold Cherenkov counters, a barrel-like arrangement of time-of-flight scintillation counters, and an electromagnetic calorimeter composed of CsI(Tl) crystals. All subdetectors were located inside a superconducting solenoid coil that provided a 1.5 T magnetic field. An iron flux-return yoke, placed outside the coil, was instrumented with resistive-plate chambers to detect K^0_L mesons and identify muons. Two inner detector configurations were used: a 2.0 cm radius beam pipe and a three-layer silicon vertex detector; and, from October 2003, a 1.5 cm radius beam pipe, a four-layer silicon vertex detector, and a small-inner-cell drift chamber [16]. In this paper, we use data from this second inner detector configuration only.

The Belle II detector [17, 18] is an upgrade with several new subdetectors designed to handle the significantly larger beam-related backgrounds of the new SuperKEKB e^+e^- collider [19]. SuperKEKB uses 7 GeV electrons and 4 GeV positrons, which results in the same c.m. energy as at KEKB. The detector consists of a silicon vertex detector wrapped around a 1.0 cm radius beam pipe that contains two inner layers of pixel detectors and four outer layers of double-sided strip detectors, a 56-layer central drift chamber, a time-of-propagation detector, and an aerogel Cherenkov detector. The Belle CsI(Tl) crystal calorimeter, the Belle solenoid, and the iron flux-return yoke are reused in the Belle II detector. The calorimeter readout electronics have been upgraded, and the endcaps of the flux-return yoke, together with the two innermost layers of the barrel, have been re-instrumented with plastic scintillator modules; the read-out system has also been upgraded. For the data used in this paper, collected between 2019 and 2022, only part of the second layer of the pixel detector, covering 15% of the azimuthal angle, was installed.

The data analysis strategy is tested on simulated event samples. We generate $e^+e^- \to \Upsilon(4S) \to B\bar{B}$ events and simulate particle decays with EvtGen, interfaced to Pythia [20]; we generate continuum $e^+e^- \to q\bar{q}$ (where q is a u, d, c, or s quark) with Pythia6 [21] for Belle, and with KKMC [22] and Pythia8 [23] for Belle II; we simulate detector response using Geant3 [24] for Belle and Geant4 [25] for Belle II.

3 Event selection

We use the Belle II analysis software framework (basf2) to reconstruct both Belle and Belle II data [26, 27]. The Belle data are converted to the Belle II format for basf2 compatibility using the B2BII framework [28].

We fully reconstruct B^0 and B^+ mesons in about 1000 exclusive hadronic final states using the Full Event Interpretation (FEI) package [29]. Background suppression in this package is based on a multivariate analysis. We use a version of the FEI adapted for energy-dependent cross-section measurements, described in refs. [9, 10].

Signal candidates peak at zero in the ΔE distribution,

$$\Delta E = E_B - \bar{E}_B, \tag{3.1}$$

where E_B is the energy of the B candidate in the e^+e^- c.m. system. The sum $\Delta E + M_{\rm bc}$ is equal to the mass of the B candidate to a high precision. Therefore, in the variable

$$\Delta E' = \Delta E + M_{\rm bc} - m_B, \tag{3.2}$$

the effect of the energy spread cancels. We select B candidates in the $\Delta E'$ signal region and sideband. In the case of Belle II, the $\Delta E'$ signal region is defined as $|\Delta E'| < 18\,\text{MeV}$, while in the case of Belle, the size of the signal region varies depending on the reconstruction channel. The efficiency of the $\Delta E'$ requirement is close to 92% for both Belle and Belle II. The sideband is shifted by $+80\,\text{MeV}$ and has the same width as the signal region and is used to constrain the background shape. The $\tilde{M}_{\rm bc}$ distributions for selected B^+ and B^0 candidates in the $\Delta E'$ signal region and sideband in the Belle and Belle II data samples are shown in figures 1 and 2.

4 $\tilde{M}_{\rm bc}$ fit function

The $\tilde{M}_{\rm bc}$ signal fit function is a key tool in this analysis. It is based on the fit functions developed in refs. [9, 10]. The fit function is calculated numerically at each minimization step and takes into account the following:

- variation of the average e^+e^- c.m. energy $\bar{E}_{\rm cm}$ over the data-taking period;[2]
- $E_{\rm cm}$ spread due to fluctuations in synchrotron radiation emission, $\sigma_{E_{\rm cm}}$;
- initial state radiation (ISR);
- energy dependence of the $e^+e^- \to B^0\bar{B}^0$ and $e^+e^- \to B^+B^-$ cross sections;
- momentum resolution of reconstructed B mesons.

[2] The change of collision energy with time was not explicitly considered in refs. [9, 10]; thus, the corresponding effect was absorbed in the energy spread.

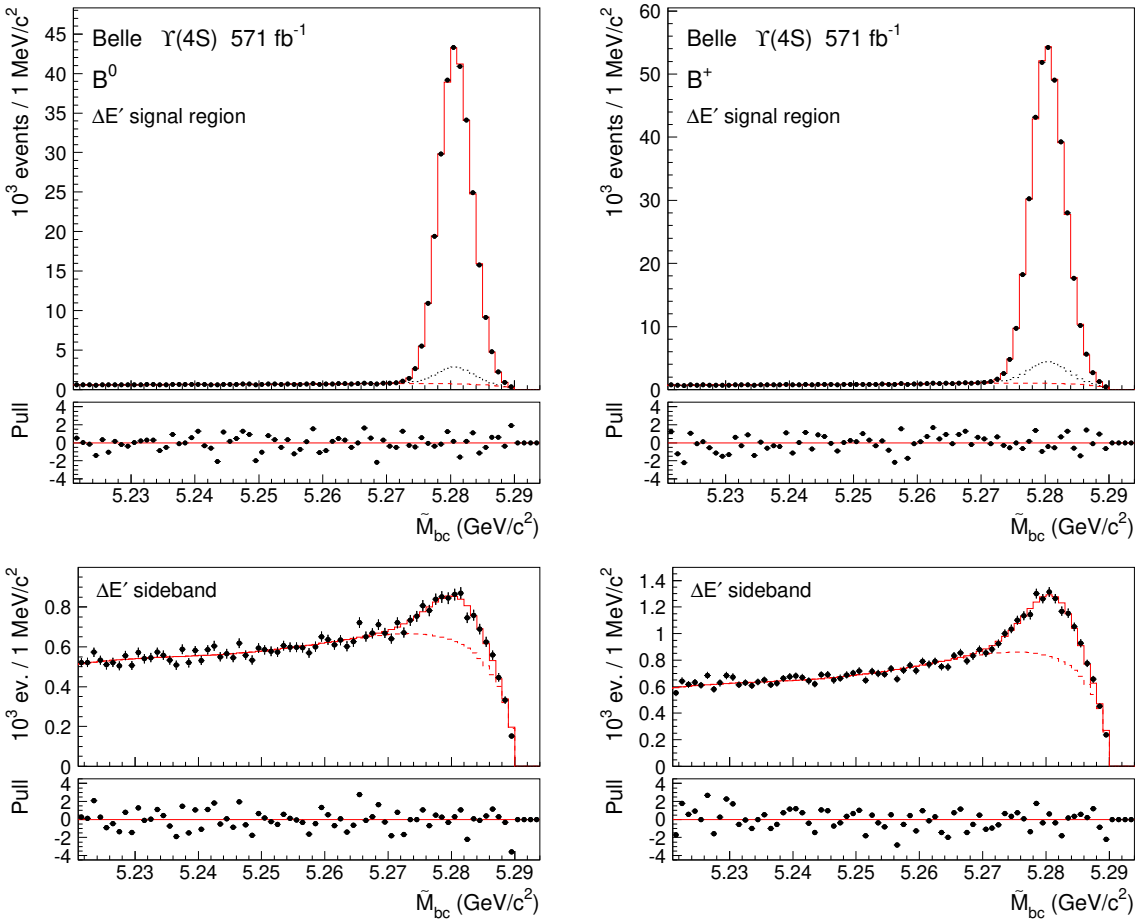

Figure 1: The $\tilde{M}_{\rm bc}$ distributions in the Belle $\Upsilon(4S)$ data for the B^0 (left) and B^+ (right) candidates. The top and bottom parts of the figure correspond to the $\Delta E'$ signal region and sideband, respectively. The red solid histogram is the result of the combined fit described in section 8. The red dashed histogram shows the background, and the black dotted histogram shows the sum of the background and the broken signal (for the $\Delta E'$ sideband, this coincides with the total fit, and is thus not visible). The bottom panels show pulls (deviations of the data points from the fit function divided by the uncertainties on the data).

The calculation scheme for the B^+ fit function is as follows:

$$[\sum_i w_{\rm i}\, G(E_{\rm cm};\ E_{\rm cm0} + \Delta E^{\rm (i)}_{\rm cm},\, \sigma_{E_{\rm cm}})] \otimes f_{\rm ISR} \times \sigma(e^+e^- \to B^+B^-)$$
$$\longmapsto f(p_{B^+}),\ \otimes f_{\rm resolution} \longmapsto f(\tilde{M}_{\rm bc}), \qquad (4.1)$$

where $G(E_{\rm cm})$ is a Gaussian representing the c.m. energy spread; $E_{\rm cm0}$ is the c.m. energy averaged over the entire running period; $\Delta E^{\rm (i)}_{\rm cm}$ is the energy deviation of the i-th data subsample; w_i is the corresponding weight (the fraction of the total sample in the i-th subsample); $\sum_i$ is the sum over different subsamples; and $\otimes f_{\rm ISR}$ represents convolution with the ISR kernel [30]. At this stage of the calculation, we obtain the distribution in the

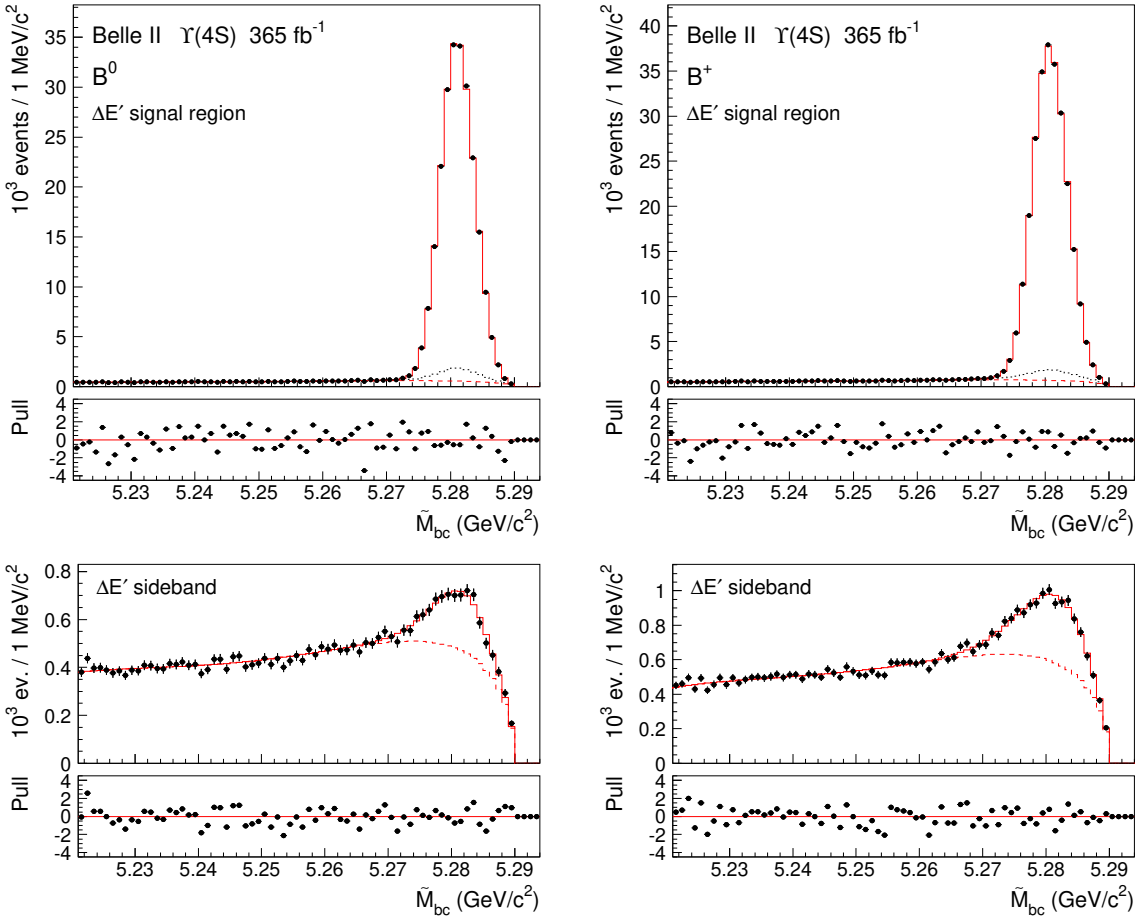

Figure 2: The $\tilde{M}_{\rm bc}$ distributions in the Belle II $\Upsilon(4S)$ data for the B^0 (left) and B^+ (right) candidates. The panels and the curves have the same meaning as in figure 1.

invariant mass of the virtual photon produced in e^+e^- annihilation. Next, we multiply this distribution by the energy dependence of the B^+B^- cross section $[\times\sigma(e^+e^- \to B^+B^-)]$, obtaining the distribution of the energy of B^+B^- pairs. We then change variables from B^+B^- energy to B^+ momentum (denoted by "$\longmapsto$"). This change takes into account nonlinear effects, which are especially important near the kinematic boundary $p_{B^+} = 0$. At this stage, the value of $m(B^+)$ enters the fit function. We perform a convolution to account for the B^+ momentum resolution ("$\otimes f_{\rm resolution}$"). Finally, we change variables from p_{B^+} to $\tilde{M}_{\rm bc}$. The fit function for B^0 is calculated in a similar way, but using the $B^0\bar{B}^0$ cross section, the B^0 mass, and the B^0 momentum-resolution.

The parameters $E_{\rm cm0}$ and $\sigma_{E_{\rm cm}}$ are determined from the combined fit. The deviations $\Delta E^{\rm (i)}_{\rm cm}$ and the weights w_i are determined using the $\tilde{M}_{\rm bc}$ fits in $\bar{E}_B$ bins (section 5 below). There are separate parameters for the Belle and Belle II data samples. The energy

dependence of the dressed cross sections[3] is parameterized as [10]

$$\sigma(e^+e^- \to B^+B^-) = p^3_{B^+}\ P_{11}(E_{\rm cm}), \tag{4.2}$$
$$\sigma(e^+e^- \to B^0\bar{B}^0) = p^3_{B^0}\ P_{11}(E_{\rm cm})\ P_2(E_{\rm cm}), \tag{4.3}$$

where $p^3_{B^0}$ and $p^3_{B^+}$ are phase-space factors, $P_{11}(E_{\rm cm})$ is an 11th order Chebyshev polynomial which is common for both cross sections, and $P_2(E_{\rm cm})$ is a second order Chebyshev polynomial that accounts for additional energy dependence of the cross-section ratio beyond the phase-space factor. All parameters of the Chebyshev polynomials are allowed to float in the combined fit. The mass of the B^+ is fixed to the average value of the Particle Data Group (PDG), $m(B^+) = (5279.42 \pm 0.08)\,{\rm MeV}/c^2$ [8], which, unlike the PDG fit value, does not include the Δm measurement of BaBar [7]. The B^0 and B^+ mass difference Δm is determined from the combined fit. Alternatively, one could fix $m(B^0)$ and vary Δm; we chose to fix $m(B^+)$ because it is 2.5 times more precise.

The B-meson momentum resolution functions are obtained from the simulation and are adjusted to take into account the difference between simulation and data. In the simulation, we find three types of events that peak in $\tilde{M}_{\rm bc}$ distributions: (1) correctly reconstructed signal candidates, (2) broken-signal candidates in the $\Delta E'$ signal region, and (3) broken-signal candidates in the $\Delta E'$ sideband. The broken signal is due to signal events in which one of the final-state particles originates from background. The momentum resolution for the correctly reconstructed candidates is described by a sum of three Gaussian functions multiplied by a factor taking into account the fact that momentum is required to be positive [10]. The broken signal components are described via a similar function but with a large width [9, 10]. The yield ratios of the broken and correctly reconstructed signal candidates are about 5% and 2% for the $\Delta E'$ signal region and sideband, respectively. The yield ratios and parameters of the momentum resolution functions are fixed using simulation (the values are provided in Refs. [9, 10]). To account for the difference between simulation and data, we introduce shifts, s_i, and broadening factors, ϕ_i, where i runs over all event types, $i = 1, 2, 3$. For broken signal, in addition we introduce normalization corrections, n_2 and n_3. There are separate corrections for B^0 and B^+, and for the Belle and Belle II data samples. The broadening factors for correctly reconstructed candidates, ϕ_1, are estimated using the fits to the $\Delta E'$ distributions in the $\tilde{M}_{\rm bc}$ signal region [9, 10]. The broadening factor of $\Delta E'$ is 1.18 ± 0.01 for Belle and 1.07 ± 0.01 for Belle II. From the simulation, we find that the broadening factor in $\Delta E'$ is larger than that in the momentum resolution by 3%. We account for this correction and fix ϕ_1 in the combined fit. We also fix $s_1 = s_2 = 0$ and $n_2 = \phi_2 = 1$, while the parameters n_3, s_3 and ϕ_3 are determined from the fit.

Combinatorial background is parameterized by the threshold function, $\sqrt{\frac{m_{\Upsilon(4S)}}{2} - \tilde{M}_{\rm bc}}$, multiplied by a second order polynomial. The shape of the combinatorial background is the same in the $\Delta E'$ signal region and sideband, while the normalizations differ. All parameters of the combinatorial background are determined from the fit.

[3] The difference between the Born and dressed cross sections is that the latter includes the vacuum polarization effect.

5 Measurement of the energy dependence of $\mathcal{R}$

The $\mathcal{R}(E_{\rm cm})$ dependence is measured using variations in the collision energy over the course of data taking. The B-meson energy is calibrated in the following way [31]: the total data sample is divided into parts corresponding to data collection periods of several days. The average energy $\bar{E}_B$ is then determined using several low-multiplicity, low-background B-decay channels. The $\bar{E}_B$ accuracy achieved for one part is typically $0.1 - 0.2\,\text{MeV}$.[4] The distribution of the selected B-meson candidates in the energy of the $B\bar{B}$ pair, $\bar{E}_{B\bar{B}} \equiv 2\,\bar{E}_B$, is shown in figure 3. The $\bar{E}_{B\bar{B}}$ values span intervals of width 4.4 MeV at Belle and 6.6 MeV at

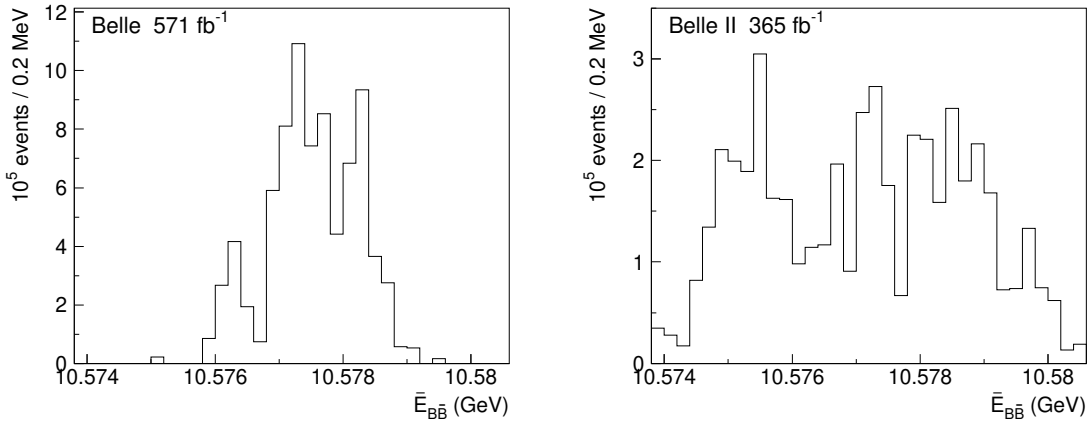

Figure 3: The distribution of B-meson candidates in the calibrated energy of the $B\bar{B}$ pair in Belle (left) and Belle II data (right).

Belle II. We subdivide the $\bar{E}_{B\bar{B}}$ range into bins of width 0.2 MeV and perform a simultaneous fit to the $\tilde{M}_{\rm bc}$ distributions of the B^0 and B^+ candidates in each bin. In the i-th bin, we fix all parameters of the $\tilde{M}_{\rm bc}$ fit function except the total B^0 and B^+ signal yield, $(N_{B^0} + N_{B^+})^{(\rm i)}$; the yield ratio, $(N_{B^0}/N_{B^+})^{(\rm i)}$; the average c.m. energy $\bar{E}^{(\rm i)}_{\rm cm}$ for a given $\bar{E}_{B\bar{B}}$ bin; the $E_{\rm cm}$ spread; and the combinatorial background yields. The results for $\bar{E}_{\rm cm}$ as a function of $\bar{E}_{B\bar{B}}$ are shown in figure 4. The values of $\bar{E}_{\rm cm}$ span intervals of 5.9 MeV and 8.1 MeV at Belle and Belle II, respectively. These intervals are wider than those of $\bar{E}_{B\bar{B}}$ by a factor of ~ 1.3. This behavior agrees with expectations based on eq. (4.1).[5] The results for the energy spread are consistent with being independent of $\bar{E}_{B\bar{B}}$ (the absolute values for Belle and Belle II are given in section 8).

The ratio of visible $e^+e^- \to B^0\bar{B}^0$ and $e^+e^- \to B^+B^-$ cross sections is determined as

$$\mathcal{R}^{(\rm i)}_{\rm v} = (N_{B^0}/N_{B^+})^{(\rm i)}\,(1/r_\varepsilon), \tag{5.1}$$

where $r_\varepsilon \equiv \varepsilon_{B^0}/\varepsilon_{B^+}$ is the ratio of the B^0 and B^+ reconstruction efficiency, the change of which with energy is negligibly small. We do not attempt to determine r_ε from simulation

[4] The calibration of the boost vector, i.e. the velocity of the c.m. system in the laboratory frame, is based on the angles of the muons in the $e^+e^- \to \mu^+\mu^-$ process [31].

[5] Indeed, in the absence of the ISR, the $\bar{E}_{B\bar{B}}$ value is always shifted from $\bar{E}_{\rm cm}$ towards the cross-section peak (the shift is zero if $\bar{E}_{\rm cm} = m_{\Upsilon(4S)}$), which shrinks the interval spanned by $\bar{E}_{B\bar{B}}$ compared to that spanned by $\bar{E}_{\rm cm}$. The effect of ISR is to further shift all the points towards lower $\bar{E}_{B\bar{B}}$ values.

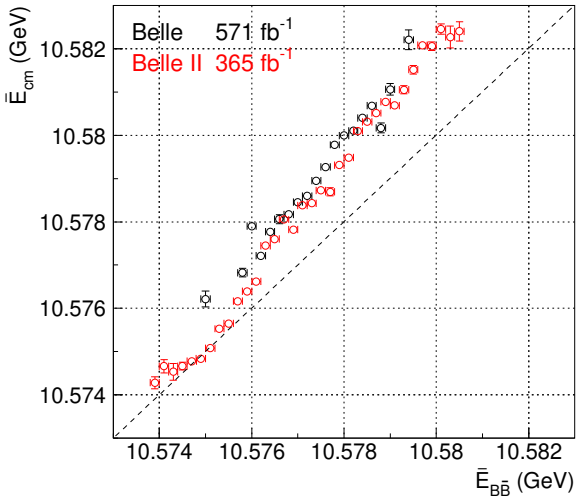

Figure 4: Energy of the colliding beams as a function of the energy of the $B\bar{B}$ pair. The black and red dots correspond to the Belle and Belle II data, respectively. Horizontal error bars indicate $\bar{E}_{B\bar{B}}$ bins, while vertical error bars show the statistical uncertainty in $\bar{E}_{\rm cm}$.

as the corresponding systematic uncertainty could be difficult to control. Instead, for the absolute normalization of $\mathcal{R}_{\rm v}$, we use the world-average value of the measurements at the energy of the $\Upsilon(4S)$ peak [32]

$$\mathcal{R}_{\rm v} = 0.951 \pm 0.028. \tag{5.2}$$

We apply the constraint of eq. (5.2) in the combined fit. The error in eq. (5.2) is accounted for as a systematic uncertainty (section 9). The values of r_ε at Belle and Belle II are determined from the combined fit.

The ratio of visible $e^+e^- \to B^0\bar{B}^0$ and $e^+e^- \to B^+B^-$ cross sections as a function of $\bar{E}_{\rm cm}$ is shown in figure 5. The Belle and Belle II results are in good agreement; there is a slight increase of $\mathcal{R}_{\rm v}$ with energy. The fit function describing the $\mathcal{R}_{\rm v}$ measurements is the ratio of visible $\sigma_{\rm v}(e^+e^- \to B^0\bar{B}^0)$ and $\sigma_{\rm v}(e^+e^- \to B^+B^-)$ cross sections that are obtained from dressed cross sections in Eqs. (4.2) and (4.3) by applying radiative corrections (convolving with the radiative kernel) and accounting for the beam-energy spread (convolving with a Gaussian) as described in refs. [9, 10].

In the $\tilde{M}_{\rm bc}$ fits in energy bins, many parameters are fixed to the result of the combined fit. To obtain self-consistent results, we use an iterative procedure. We perform a combined fit, fix parameters and perform $\tilde{M}_{\rm bc}$ fits in $\bar{E}_B$ bins to measure $\mathcal{R}_{\rm v}$. The latter results are used in the next iteration. The fit converges after two iterations.

To estimate the systematic uncertainties in $\mathcal{R}_{\rm v}^{\rm (i)}$ due to uncertainties in the parameters that are fixed in the $\tilde{M}_{\rm bc}$ fits, we use a pseudo-experiment technique. We generate pseudo-experiments using the fitted function that is obtained from the combined fit (section 8). We then perform a combined fit to the pseudo-experiments and use the results to fix the parameters of the $\tilde{M}_{\rm bc}$ fits in $\bar{E}_{B\bar{B}}$ bins. We repeat the measurements of $\mathcal{R}_{\rm v}$ in $\bar{E}_{B\bar{B}}$ bins using parameters of each pseudo-experiment. We treat the RMS of the deviations of $\mathcal{R}_{\rm v}^{\rm (i)}$ as a systematic uncertainty, which is found to be negligibly small.

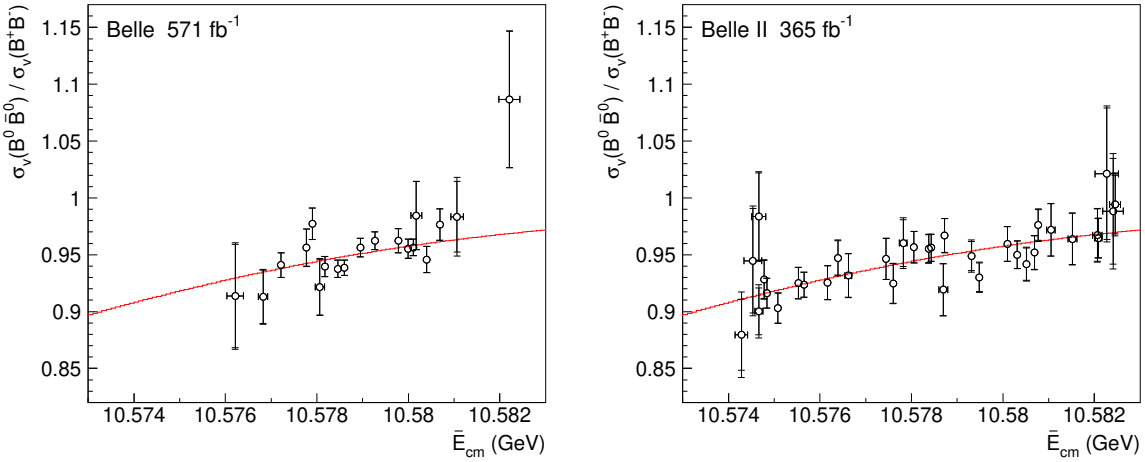

Figure 5: Energy dependence of the ratio of visible cross sections $\sigma_{\rm v}(e^+e^- \to B^0\bar{B}^0) \,/\, \sigma_{\rm v}(e^+e^- \to B^+B^-)$. The dots with error bars show the direct measurements performed using Belle (left) and Belle II (right) data; the vertical inner and outer error bars show statistical and total uncorrelated uncertainties, respectively; the horizontal error bars show statistical uncertainty. The curve is the result of the combined fit described in section 8.

To estimate the systematic uncertainty due to the modelling of the smooth background, we float the parameters of the corresponding polynomial in the fits in the $\bar{E}_{B\bar{B}}$ bins. Deviations of $\mathcal{R}_{\rm v}^{\rm (i)}$ are treated as symmetric systematic uncertainties. These uncertainties are small compared to statistical uncertainties and are assumed to be uncorrelated for different $\bar{E}_{B\bar{B}}$ bins. The total uncertainty is obtained by summing the statistical and systematic contributions in quadrature. The total and statistical uncertainties are shown in figure 5.

6 R_b fit function

BaBar reported the most precise measurement of the total visible $e^+e^- \to b\bar{b}$ cross section in the $\Upsilon(4S)$ energy region [11]. The results were presented in terms of R_b,

$$R_b = \frac{\sigma_{\rm v}(e^+e^- \to b\bar{b})}{\sigma_0}, \tag{6.1}$$

where $\sigma_0 = \frac{4\pi\alpha}{3}\,\frac{1}{E_{\rm cm}^2}$ is the Born-level $e^+e^- \to \mu^+\mu^-$ cross section, and α is the QED fine-structure constant. The results of the BaBar scan for R_b are shown in figure 6. As in the previous publications [9, 10], we include the BaBar measurements of R_b at nine energies between the $B\bar{B}$ and $B\bar{B}^*$ thresholds into the combined fit. The fit function describing the energy dependence of R_b is $[\sigma_{\rm v}(e^+e^- \to B^0\bar{B}^0) + \sigma_{\rm v}(e^+e^- \to B^+B^-)]/\sigma_0$. The BaBar scan points have a rather large energy scale uncertainty of 1.5 MeV [7]. We allow all the R_b points to be shifted simultaneously along the horizontal axis by a parameter $\Delta E_{\rm BaBar}$, which is included in the fit with a Gaussian constraint around zero and a width of $\sigma = 1.5\,{\rm MeV}$.

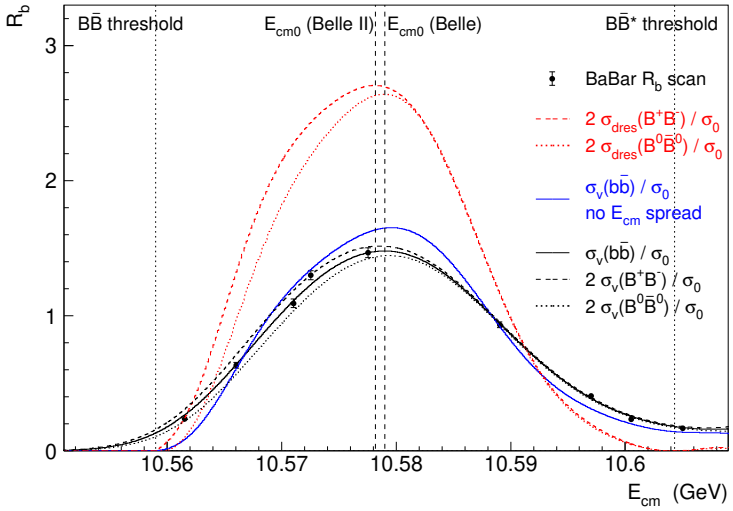

Figure 6: Energy dependence of R_b. The points with error bars are measurements from BaBar [11]. The black solid curve is the result of the combined fit described in section 8; the black dashed and dotted curves are the contributions of B^+ and B^0, respectively, multiplied by a factor of two; the blue solid curve corresponds to the visible cross section before accounting for the E_cm spread; the red dashed and dotted curves correspond to the dressed cross sections of the B^+ and B^0 production, respectively, multiplied by a factor of two. The vertical dashed lines show the average over the data taking period c.m. energies of Belle (right) and Belle II (left), the vertical dotted lines indicate the $B\bar{B}$ and the $B\bar{B}^*$ thresholds.

7 Measurement of the energy dependence of $\sigma(e^+e^- \to b\bar{b} \to D^0/\bar{D}^0\, X)$

In this analysis, the combined fit includes the energy dependence of the inclusive $e^+e^- \to b\bar{b} \to D^0\, X$ cross section. This helps to constrain the peak position of the R_b scan [11], which otherwise has a large uncertainty as noted in the previous section. We measure the energy dependence of the cross section using, as in the case of $\mathcal{R}$, variations of E_cm over the data-taking period. We use an approach in which the luminosity of data samples at various energies is determined using the yield of $e^+e^- \to c\bar{c} \to D^0\, X$. In this approach, the uncertainties due to changes in the detector performance over the data taking period largely cancel.

To measure the $e^+e^- \to b\bar{b} \to D^0/\bar{D}^0\, X$ cross section, we reconstruct $D^0 \to K^-\pi^+$ decays in the $\Upsilon(4S)$ data of Belle II. The K^- and π^+ candidates must originate from the interaction region and be positively identified based on the energy-loss measurements in the drift chamber and the response of the particle identification systems. The selection requirements are the same as in ref. [33].

For each $\bar{E}_{B\bar{B}}$ bin, we determine the D^0 yields in the $x_p < 0.5$ and $x_p > 0.55$ regions, $N^{(\mathrm{i})}_{\text{low-}x_p}$ and $N^{(\mathrm{i})}_{\text{high-}x_p}$. The normalized momentum x_p is defined as $x_p = p_D/p_D^{\max}$, where p_D is the c.m. momentum of the D^0 candidate, $p_D^{\max}$ is the maximal kinematically allowed value of p_D, $p_D^{\max} = \sqrt{(\bar{E}_\mathrm{cm}/2)^2 - m_D^2}$, and m_D is the D^0-meson world-average mass [8]. For D^0

mesons produced in $e^+e^- \to b\bar{b}$ events, x_p is below 0.55 [33]. In the case of continuum $e^+e^- \to c\bar{c}$, D^0 mesons are produced in the entire x_p range from 0 to 1. The visible $e^+e^- \to b\bar{b} \to D^0\,X$ cross section for the i-th $\bar{E}_{B\bar{B}}$ bin is calculated as

$$\sigma_{\rm v}^{\rm (i)}(e^+e^- \to b\bar{b} \to D^0\,X) \propto \frac{N^{\rm (i)}_{\text{low-}\,x_p} - r_{\rm cont}\,N^{\rm (i)}_{\text{high-}\,x_p}}{N^{\rm (i)}_{\text{high-}\,x_p}\,E^2_{\rm cm}}. \tag{7.1}$$

Here the D^0 yield in the $x_p > 0.55$ region is used both to subtract the $e^+e^- \to c\bar{c} \to D^0\,X$ continuum (the factor $r_{\rm cont}$ is the ratio of the continuum yields in the $x_p < 0.5$ and $x_p > 0.55$ regions) and for normalization (the factor $E^2_{\rm cm}$ accounts for the fact that the cross section of the continuum process is proportional to $1/E^2_{\rm cm}$).

We fit the $M(K^-\pi^+)$ distributions for the $x_p < 0.5$ and $x_p > 0.55$ regions for the entire $\bar{E}_{B\bar{B}}$ interval with a sum of three Gaussian functions and a first order polynomial. We then fit the $M(K^-\pi^+)$ distributions in $\bar{E}_{B\bar{B}}$ bins by fixing the parameters of the Gaussian functions and introducing a common shift and broadening factor that are free in the fit. The parameters of the background function are also allowed to float. An example of the fit to the $M(K^-\pi^+)$ distributions in the 4th $\bar{E}_{B\bar{B}}$ bin is shown in figure 7 (the $\bar{E}_{B\bar{B}}$ bins are shown in figure 3).

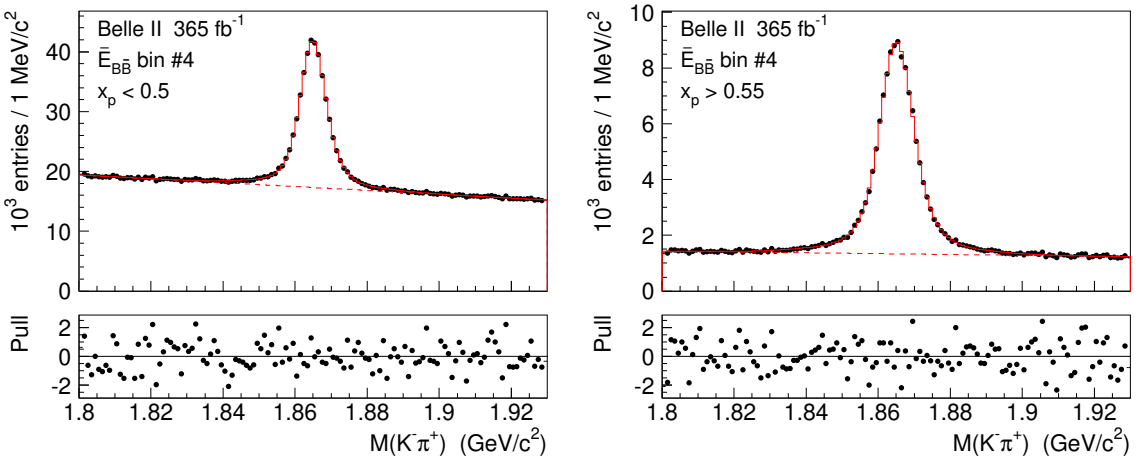

Figure 7: The $M(K^-\pi^+)$ distributions for D^0 candidates with $x_p < 0.5$ (left) and $x_p > 0.55$ (right) in the 4th $\bar{E}_{B\bar{B}}$ bin. The solid histogram is the result of the fit; the dashed histogram is the background component of the fit.

The factor $r_{\rm cont}$ is determined using fits to the $M(K^-\pi^+)$ distributions in an off-resonance data sample that has an integrated luminosity of 43 fb^{-1}, collected at $E_{\rm cm} = 10.52$ GeV. We find $r_{\rm cont} = 0.608 \pm 0.006$. The result for the visible $e^+e^- \to b\bar{b} \to D^0/\bar{D}^0\,X$ cross section in arbitrary units is shown in figure 8.

In the combined fit, the visible $e^+e^- \to b\bar{b} \to D^0/\bar{D}^0\,X$ cross section is described by the function

$$\begin{aligned}\sigma_{\rm v}(e^+e^- \to b\bar{b} \to D^0/\bar{D}^0\,X) = {} & \sigma_{\rm v}(e^+e^- \to B^+B^-)\;2\,\mathcal{B}(B^+ \to D^0/\bar{D}^0\,X) + \\ & \sigma_{\rm v}(e^+e^- \to B^0\bar{B}^0)\;\;2\,\mathcal{B}(B^0 \to D^0/\bar{D}^0\,X).\end{aligned}$$

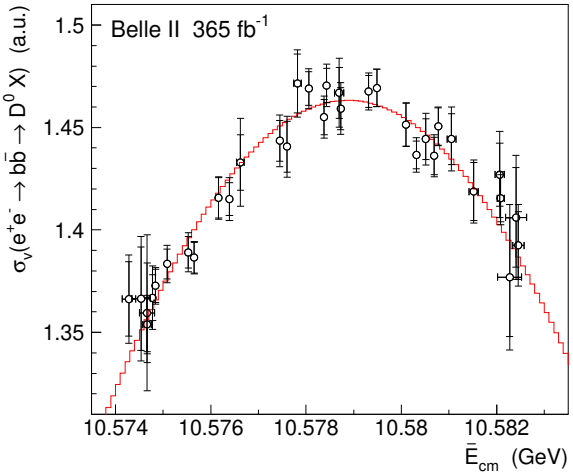

Figure 8: Visible $e^+e^- \to b\bar{b} \to D^0/\bar{D}^0\, X$ cross section versus $\bar{E}_{\rm cm}$. The open circles with error bars show the direct measurement performed using Belle II data; the inner and outer error bars show statistical and total uncorrelated uncertainties, respectively. The curve is the result of the combined fit described in section 8. The vertical scale is in arbitrary units.

We use the world-average values [8]

$$\mathcal{B}(B^+ \to D^0/\bar{D}^0\, X) = (87.6 \pm 4.1)\%, \tag{7.2}$$

$$\mathcal{B}(B^0 \to D^0/\bar{D}^0\, X) = (55.5 \pm 3.2)\%. \tag{7.3}$$

Since the vertical scale in figure 8 is arbitrary, we multiply the fit function by a normalization parameter, which is free in the fit.

To account for the uncertainties in $\bar{E}_{\rm cm}$, $\delta(E_{\rm cm})$, we use the formula

$$\delta\sigma_{\rm v} = |f'(E_{\rm cm})|\, \delta(E_{\rm cm}), \tag{7.4}$$

where $f'(E_{\rm cm})$ is the derivative of the $\sigma_{\rm v}(e^+e^- \to b\bar{b} \to D^0/\bar{D}^0\, X)$ dependence on $E_{\rm cm}$. At the boundaries of the $\bar{E}_{\rm cm}$ range, where the values of $|f'(E_{\rm cm})|$ are large, the contribution of the $\bar{E}_{\rm cm}$ uncertainty is up to 40% of the statistical uncertainty in the cross section. In the case of the $\mathcal{R}_{\rm v}$ energy dependence described in section 5, the contribution of the uncertainty in $\bar{E}_{\rm cm}$ is negligibly small.

To estimate the systematic uncertainty associated with the signal shape, we introduce additional corrections: a shift and broadening for the sum of the second and third Gaussians in the parameterization of the signal shape. These two Gaussians account for about 50% of the signal yield. To estimate the systematic uncertainty associated with the background modeling, we change the order of the polynomial that parameterizes the background shape from first to second. We repeat the fits and consider deviations as symmetric systematic uncertainties, which are assumed to be uncorrelated between $\bar{E}_{B\bar{B}}$ bins. The uncertainties from the two sources are comparable. To obtain the total uncertainty, we add in quadrature the statistical uncertainty, the contribution due to the uncertainty in $E_{\rm cm}$, and the systematic contributions. The total and statistical uncertainties are shown in figure 8.

The $e^+e^- \to b\bar{b} \to D^0/\bar{D}^0\,X$ cross-section measurements at Belle cover a smaller energy range than at Belle II. They agree with the expectations based on the combined fit but do not provide a significant constraint on the cross-section peak position. For simplicity, we do not include the $e^+e^- \to b\bar{b} \to D^0/\bar{D}^0\,X$ cross-section measurement at Belle in the combined fit.

8 Combined fit and its results

We perform a simultaneous fit to the distributions shown in figures 1, 2, 5, 6 and 8. The corresponding fit functions are described in the previous sections. The fits to $\tilde{M}_{\rm bc}$ distributions are binned likelihood ($-2\ln L$) fits, while the fits to the energy dependence of the R_b, B^0/B^+ cross-section ratio and $\sigma(e^+e^- \to b\bar{b} \to D^0/\bar{D}^0\,X)$ are χ^2 fits. The $-2\ln L$ and χ^2 values are added together and their sum is passed to the fit for minimization. The results are shown in these figures and in tables 1, 2 and 3. Throughout this paper, the first uncertainty is statistical and the second, if present, is systematic. The tables show the

Table 1: Fit results for Δm and the c.m. energy-related variables.

Δm	$(0.495 \pm 0.024 \pm 0.005)\,\mathrm{MeV}/c^2$
Belle	
$E_{\rm cm0}$	$(10579.05 \pm 0.04 \pm 0.18)\,\mathrm{MeV}$
$\sigma_{E_{\rm cm}}$	$(5.35 \pm 0.07 \pm 0.09)\,\mathrm{MeV}$
Belle II	
$E_{\rm cm0}$	$(10578.19 \pm 0.05 \pm 0.22)\,\mathrm{MeV}$
$\sigma_{E_{\rm cm}}$	$(5.24 \pm 0.08 \pm 0.15)\,\mathrm{MeV}$
$\Delta E_{\rm BaBar}$	$(-1.27 \pm 0.14 \pm 0.22)\,\mathrm{MeV}$

Table 2: Fit results for the B^+ and B^0 signal yields and the efficiency ratio.

	Belle	Belle II
$N_{B^+} + N_{B^0}$	$(587.6 \pm 0.8) \cdot 10^3$	$(458.2 \pm 0.7) \cdot 10^3$
$N_{B^0}\ /\ N_{B^+}$	0.789 ± 0.002	0.895 ± 0.003
r_ε	0.830 ± 0.002	0.949 ± 0.003

results for 24 fit parameters. In addition, there are 12 free parameters describing the R_b energy dependence, 3 parameters describing $\mathcal{R}(E_{\rm cm})$, 20 parameters describing the yields and shapes of smooth background in the $\tilde{M}_{\rm bc}$ distributions, and an additional parameter describing the normalization of the $\sigma(D^0/\bar{D}^0\,X)$ measurement. Thus, there are a total of 60 free parameters in the fit. All distributions are described well by the fit functions. The results for $E_{\rm cm0}$ and $\sigma_{E_{\rm cm}}$ at Belle, and $\Delta E_{\rm BaBar}$ are in agreement with the Belle-only

Table 3: Fit results for the peaking background corrections.

	Belle		Belle II	
	B^+	B^0	B^+	B^0
n_3	1.22 ± 0.07	1.20 ± 0.13	1.03 ± 0.06	1.13 ± 0.09
s_3, MeV/c	-5.8 ± 2.7	-3.0 ± 4.4	15.0 ± 3.1	17.0 ± 3.9
ϕ_3	0.84 ± 0.06	1.02 ± 0.12	0.64 ± 0.04	0.53 ± 0.05

results [9]. The fitted values of $\sigma(b\bar{b})$ and $\mathcal{R}$ as functions of $E_{\rm cm}$ with a step size of 0.1 MeV are given in appendix A. We also provide fitted values for pseudo-experiments and fit modifications for the main sources of systematic uncertainty. This information can be used to perform energy calibration near the $\Upsilon(4S)$ peak or for phenomenological studies.

9 Systematic uncertainties and additional studies

The contributions to the systematic uncertainty in the fit results are shown in table 4. We

Table 4: Systematic uncertainties from various sources in Δm (in MeV/c^2), $E_{\rm cm0}$ and $\sigma_{E_{\rm cm}}$ (for Belle and Belle II), and $\Delta E_{\rm BaBar}$ (in MeV).

	Δm	Belle		Belle II		$\Delta E_{\rm BaBar}$
		$E_{\rm cm0}$	$\sigma_{E_{\rm cm}}$	$E_{\rm cm0}$	$\sigma_{E_{\rm cm}}$	
B^+ mass	0.001	0.160	0.011	0.160	0.013	0.163
Absolute value of $\mathcal{R}_{\rm v}$	0.002	0.007	0.007	0.008	0.008	0.009
$\mathcal{B}(B \to D^0/\bar{D}^0\, X)$	0.001	0.005	0.001	0.005	0.002	0.008
R_b vs. $E_{\rm cm}$ parameterization	0.000	0.040	0.040	0.040	0.052	0.071
$\mathcal{R}$ vs. $E_{\rm cm}$ parameterization	0.001	0.048	0.046	0.044	0.060	0.086
Momentum scale	0.001	0.002	0.000	0.001	0.000	0.002
Momentum resolution	0.002	0.007	0.005	0.043	0.045	0.012
Peaking background	0.003	0.023	0.053	0.127	0.114	0.051
Smooth background	0.000	0.047	0.029	0.042	0.037	0.078
Binning	0.002	0.004	0.004	0.001	0.006	0.003
Total	0.005	0.180	0.087	0.221	0.151	0.219

consider the following sources of systematics uncertainties.

1. **Uncertainty in the B^+ mass.** For the B^+ mass, we use the PDG average (not the PDG fit): $m(B^+) = (5279.42 \pm 0.08)\,\text{MeV}/c^2$ [8]. We vary its value by ± 1 standard deviation and repeat the analysis. Here and in all cases described below, we estimate

the systematic uncertainty as the maximum deviation of the fit result, assuming that the systematic uncertainties are symmetric.

2. **Uncertainty in the absolute value of $\mathcal{R}_v$.** We vary the world-average value $\mathcal{R}_v = 0.951 \pm 0.028$ [32] measured at the $\Upsilon(4S)$ peak by its uncertainty.

3. **Uncertainty in $\mathcal{B}(B \to D^0/\bar{D}^0 X)$.** We vary the values of $\mathcal{B}(B^+ \to D^0/\bar{D}^0 X) = (87.6 \pm 4.1)\%$ and $\mathcal{B}(B^0 \to D^0/\bar{D}^0 X) = (55.5 \pm 3.2)\%$ [8] by their uncertainties. The contributions from B^0 and B^+ are added in quadrature.

4. **Parameterization of R_b energy dependence.** In the default fit, the energy dependence of R_b is parameterized by an 11th order Chebyshev polynomial. We also fit with 12th and 13th orders as a cross-check.

5. **Parameterization of $\mathcal{R}$ energy dependence.** We find that a second order Chebyshev polynomial is sufficient to describe the $\mathcal{R}$ energy dependence; increasing the order gives a very small reduction of the overall $\chi^2 - 2\ln L$ of the fit. We consider polynomial orders up to 10. The results of the fits with different polynomial orders for the ratio of visible and dressed cross sections are shown in figure 9. In the same figure, we

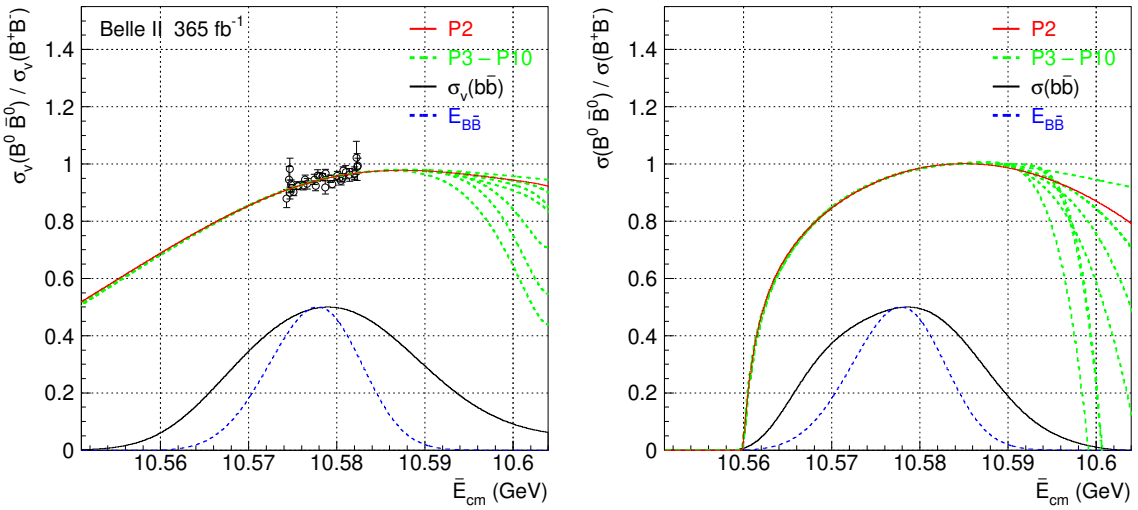

Figure 9: (Left) the ratio of visible cross sections $\sigma_v(e^+e^- \to B^0\bar{B}^0) \,/\, \sigma_v(e^+e^- \to B^+B^-)$ versus energy. The open circles with error bars show the direct measurement using Belle II data; the red solid curve is the result of the nominal fit; the green dashed curves correspond to the orders of the polynomial describing the $\mathcal{R}$ energy dependence from three to 10; the black solid curve shows the energy dependence of the visible $e^+e^- \to B\bar{B}$ cross section; the blue dashed curve shows the distribution of the number of produced $B\bar{B}$ pairs. Normalization (vertical scale) of the latter two curves is arbitrary. (Right) the same curves as on the left panel, except that they correspond to dressed cross sections before accounting for the energy spread.

also show the energy dependence of the $e^+e^- \to b\bar{b}$ cross section and the distribution

of the number of produced $B\bar{B}$ pairs, which corresponds to the first line of eq. (4.1). The curves corresponding to different polynomial orders coincide in the energy region covered by $E_{B\bar{B}}$, but begin to diverge outside this region. This is because the $\tilde{M}_{\rm bc}$ distributions constrain the cross-section shapes in the region covered by $E_{B\bar{B}}$.

6. **Uncertainty in the momentum scale.** We find that the $\Delta E'$ peak positions differ slightly between simulation and data. We introduce momentum-scale corrections in the simulation to reproduce the peak positions in the data.

7. **Uncertainty in the momentum resolution.** We vary the correction factors ϕ_1 for the width of the momentum resolution function by $\pm 3\%$, which is the relative difference of the width correction factors for the $\Delta E'$ and momentum resolutions (section 4).

8. **Modelling of peaking background.** We have two types of peaking background: in the $\Delta E'$ signal region and in the $\Delta E'$ sideband. The shapes of these backgrounds and their yield relative to the signal events are determined from simulation. In the default model, we introduce correction parameters for the peaking component in the sideband, n_3, s_3 and ϕ_3 (for yield, peak position and broadening), while corrections for the peaking background in the $\Delta E'$ signal region are fixed at the values $n_2 = 1$, $s_2 = 0$ and $\phi_2 = 1$. We consider two alternative peaking background models. In the first, we assume $n_2 = n_3$, $s_2 = s_3$ and $\phi_2 = \phi_3$, and treat these as free parameters in the fit. In the second model, the parameters n_2, s_2 and ϕ_2 are varied independently in the fit. The peaking background is enhanced in channels with $D^*_{(s)}$ due to soft pions or γ's from $D^*_{(s)}$ decays. We exclude all such channels when plotting the $\tilde{M}_{\rm bc}$ distributions. We lose 1/2 (1/3) of the B^0 (B^+) sample, while the peaking-background fraction is reduced by about a factor of 2.5. We then repeat the combined fit. In all cases, the changes in Δm are small (table 4).

9. **Modelling of smooth background.** The smooth background is described by a second order polynomial multiplied by a threshold function; we increase the order of the polynomial by one.

10. **Binning.** We shift the binning in $\tilde{M}_{\rm bc}$ distributions (figures 1 and 2) and in $\bar{E}_{B\bar{B}}$ distributions (figure 3) by half the bin size.

The change in Δm is negligible when $m(B^0)$ is used as an external parameter instead of $m(B^+)$. Based on the results in table 4, any change in Δm arising from future improvements in the knowledge of $m(B^+)$ or the absolute value of $\mathcal{R}_{\rm v}$ would be negligible compared to the statistical uncertainty of $0.024\,{\rm MeV}/c^2$, and no adjustment of Δm will be needed.

To test how the various distributions used in the combined fit affect the precision in Δm, we perform the fit excluding some distributions. The uncertainty in Δm changes very little if we exclude the $\tilde{M}_{\rm bc}$ distributions of Belle or Belle II. In contrast, the precision in Δm deteriorates significantly if either Belle or Belle II data on $\mathcal{R}_{\rm v}(E_{\rm cm})$ are excluded. If the $\mathcal{R}_{\rm v}$ data of both experiments are excluded, the uncertainty in Δm increases to $0.10\,{\rm MeV}/c^2$.

Thus, it is the slope of $\mathcal{R}$ versus $E_{\rm cm}$ that determines the precision in Δm. If we exclude the $\sigma(e^+e^- \to D^0/\bar{D}^0\,X)$ measurement, the statistical uncertainty of $E_{\rm cm0}$ in Belle and Belle II increases by a factor of 4; the statistical uncertainty of $\Delta E_{\rm BaBar}$ also increases, while all other results remain unchanged. In all cases, we find that the results with some measurements excluded are consistent with the nominal fit.

The measured value of Δm, $(0.495 \pm 0.024 \pm 0.005)\,{\rm MeV}/c^2$, differs significantly from the BaBar result, $(0.33 \pm 0.05 \pm 0.03)\,{\rm MeV}/c^2$ [7]. To study the origin of this difference, we perform the combined fit using, as in ref. [7], the phase-space hypothesis, $\mathcal{R} = (p_{B^0}/p_{B^+})^3$. The change in $\chi^2 - 2\ln L$ of the fit is $+113.1$ with the dominant contribution, $+95.5$, coming from the $\tilde{M}_{\rm bc}$ distributions (the signal fit function is too broad for B^0 and too narrow for B^+). Based on Wilks' theorem, the phase-space hypothesis is disfavored at about the $10\,\sigma$ level.[6] The value of Δm from this phase-space hypothesis fit is $(0.386 \pm 0.006)\,{\rm MeV}/c^2$, which is consistent with the BaBar result [7]. Thus, the difference in Δm (table 1) with respect to BaBar is probably due to the fact that BaBar used the phase-space hypothesis for the energy dependence of $\mathcal{R}$, which we find to be excluded.

Comparing the left and right panels in figure 9, we see that the ratio of dressed cross sections $\mathcal{R}$ reaches 1.0 while the ratio of visible cross sections $\mathcal{R}_{\rm v}$ remains a few per cent below one. This shows the importance of the ISR and energy-spread effects for the absolute value of the cross-section ratio.

10 Measurement of the ratio of dressed $B^0\bar{B}^0$ to B^+B^- cross sections in a wide energy range

The combined fit constrains the energy dependence of the dressed cross-section ratio $\mathcal{R}$ in a much wider range than that covered by direct measurement (figure 9). This is because the $\tilde{M}_{\rm bc}$ spectra of B^0 and B^+ candidates contain information about the shapes of $B^0\bar{B}^0$ and B^+B^- cross sections, as discussed in section 1. To provide information about the energy dependence of $\mathcal{R}$ for phenomenological studies, we measure $\mathcal{R}$ in $E_{\rm cm}$ bins using the combined fit. The idea is similar to the Argand plot measurement in amplitude analyses [34, 35]. The dressed cross-section ratio corrected for the phase-space factor, $\mathcal{R}(E_{\rm cm})/(p_{B^0}/p_{B^+})^3$, is described by a second order polynomial $P_2(E_{\rm cm})$ in the combined fit (eq. (4.3)). We modify the combined fit, and instead of $P_2(E_{\rm cm})$, we use a piecewise step function where the height of each step is determined from the fit. The quantity $\mathcal{R}(E_{\rm cm})/(p_{B^0}/p_{B^+})^3$ is particularly convenient for this approach, since it changes relatively slowly with energy. We chose bins of width 2.5 MeV, which results in 13 bins in the energy range $10.56 - 10.5925\,{\rm GeV}$. For the small fraction of events outside this range, we use the values in the first or last bin. The original polynomial $P_2(E_{\rm cm})$ and the results of the modified fit are shown in figure 10.

To better control the correlations among the $\mathcal{R}(E_{\rm cm})/(p_{B^0}/p_{B^+})^3$ measurements, the Δm value is fixed in the combined fit, and the uncertainty in Δm is taken into account as systematic uncertainty. We also consider the absolute value of $\mathcal{R}_{\rm v}$ (eq. (5.2)) as a source of correlated systematic uncertainty. Other sources of systematic uncertainty (table 4) have

[6] The difference in the number of degrees of freedom of the two hypotheses is three; it is the number of free parameters of $P_2(E_{\rm cm})$ in eq. (4.3).

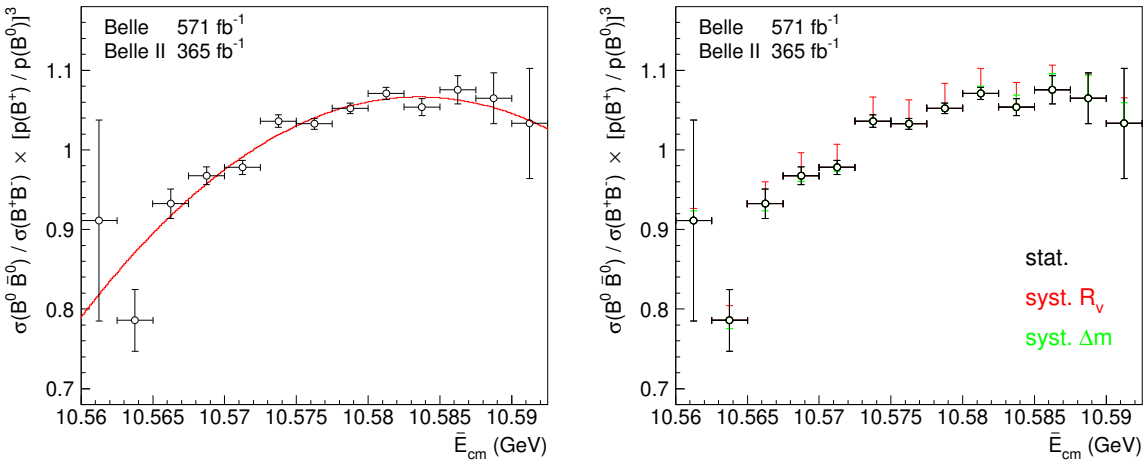

Figure 10: Energy dependence of the ratio of dressed $e^+e^- \to B^0\bar{B}^0$ and $e^+e^- \to B^+B^-$ cross sections divided by the phase-space factor $(p_{B^0}/p_{B^+})^3$. The open circles with error bars show the results of the modified combined fit; the red curve (left) shows the original second-order polynomial; the red and green error bars (right) show the systematic shifts due to variation of, respectively, $\mathcal{R}_\mathrm{v}$ and Δm by $+1$ standard deviation. The shifts due to $-1\,\sigma$ variations are not shown to make the signs of the shifts clear.

negligible influence on $\mathcal{R}$. The values of $\mathcal{R}/(p_{B^0}/p_{B^+})^3$ with statistical and systematic uncertainties for different E_cm bins are given in table 5. The correlation matrix for the measured $\mathcal{R}/(p_{B^0}/p_{B^+})^3$ values is shown in table 6.

11 Phenomenological analysis of $\mathcal{R}$ versus E_cm

To fit the data shown in figure 10, we use the phenomenological model of refs. [2, 36]. In this model, the strong interaction between $B\bar{B}$ mesons is described by a potential that has a constant value (V_1 for the isovector component) inside an interaction region of radius a and zero outside. At distances $r < a$ the wave functions of B and $\bar{B}$ overlap, so that it is impossible to distinguish the $B^0\bar{B}^0$ and B^+B^- pairs. Therefore, at $r < a$ the electromagnetic interaction is switched off in the model. The model has two parameters: the interaction range a and the $B\bar{B}$ scattering phase in the isovector channel δ_1. The scattering phase is proportional to the isovector potential V_1 and varies with E_cm; as a fit parameter, we take the δ_1 value at $E_\mathrm{cm} = 10.58\,\mathrm{GeV}$. The model is valid when $|\mathcal{R} - 1| \ll 1$, so in the fitting we exclude the two lowest energy points. We also exclude the highest energy point because it contains all events above 10.59 GeV, and hence its argument is not well defined; moreover, the corresponding uncertainty in $\mathcal{R}/(p_{B^0}/p_{B^+})^3$ is poor. Detailed information about the model, as well as the expression for $\mathcal{R}$, are given in appendix B.

We define the pull of each experimental measurement, $x_i \pm \sigma_i$ $(i = 1, 10)$, relative to the fitted value, μ_i, as

$$p_i = (x_i + \sum_{j=1}^{2} \xi_j \, \Delta x_{ji} - \mu_i)/\sigma_i \,. \tag{11.1}$$

Table 5: Measured values of the dressed cross-section ratio corrected for the phase-space factor, $\mathcal{R}/(p_{B^0}/p_{B^+})^3$, at various energies. Shown are the $E_{\rm cm}$ interval (in MeV), the central value of $\mathcal{R}/(p_{B^0}/p_{B^+})^3$ with its statistical uncertainty, and the systematic shifts from changing the $\mathcal{R}_{\rm v}$ and Δm values by $\pm 1\,\sigma$.

N	$E_{\rm cm}$ interval	$\mathcal{R}/(p_{B^0}/p_{B^+})^3$	syst. $\mathcal{R}_{\rm v}$	syst. Δm
1	10561.25 ± 1.25	0.9111 ± 0.1261	± 0.0152	± 0.0121
2	10563.75 ± 1.25	0.7858 ± 0.0389	± 0.0185	∓ 0.0104
3	10566.25 ± 1.25	0.9323 ± 0.0183	± 0.0274	∓ 0.0088
4	10568.75 ± 1.25	0.9674 ± 0.0112	± 0.0292	∓ 0.0068
5	10571.25 ± 1.25	0.9779 ± 0.0090	± 0.0291	∓ 0.0049
6	10573.75 ± 1.25	1.0362 ± 0.0077	± 0.0303	∓ 0.0029
7	10576.25 ± 1.25	1.0327 ± 0.0067	± 0.0302	± 0.0014
8	10578.75 ± 1.25	1.0524 ± 0.0066	± 0.0311	± 0.0041
9	10581.25 ± 1.25	1.0709 ± 0.0076	± 0.0318	± 0.0094
10	10583.75 ± 1.25	1.0537 ± 0.0108	± 0.0311	± 0.0152
11	10586.25 ± 1.25	1.0755 ± 0.0176	± 0.0312	± 0.0202
12	10588.75 ± 1.25	1.0647 ± 0.0320	± 0.0305	± 0.0292
13	10591.25 ± 1.25	1.0333 ± 0.0692	± 0.0320	± 0.0260

Table 6: Correlation matrix for the 13 measured values of $\mathcal{R}/(p_{B^0}/p_{B^+})^3$ shown in figure 10.

1.00	−0.24	0.16	−0.01	0.03	−0.10	0.07	−0.05	0.00	−0.02	0.01	0.03	0.07
	1.00	−0.21	0.11	−0.07	−0.04	−0.02	−0.02	−0.05	0.02	−0.02	−0.01	0.01
		1.00	−0.22	0.08	−0.12	−0.03	−0.01	−0.03	−0.01	−0.02	−0.04	0.11
			1.00	−0.23	0.10	−0.14	−0.02	−0.06	0.02	−0.03	−0.02	−0.01
				1.00	−0.43	0.18	−0.17	−0.00	−0.07	−0.01	−0.01	−0.00
					1.00	−0.45	0.16	−0.18	−0.00	−0.03	0.00	−0.07
						1.00	−0.52	0.15	−0.18	−0.03	−0.01	−0.05
							1.00	−0.54	0.19	−0.16	0.01	0.01
								1.00	−0.50	0.21	−0.13	−0.00
									1.00	−0.54	0.24	−0.20
										1.00	−0.51	0.21
											1.00	−0.39
												1.00

Here the second term takes into account systematic uncertainties due to external parameters: Δx_{ji} is the signed deviation of x_i when the j-th external parameter changes by $+1$ standard deviation (j runs over the $\mathcal{R}_{\rm v}$ and Δm contributions); ξ_j is a nuisance parameter that is free in the fit. The χ^2 of the fit is defined as [32]

$$\chi^2 = \sum_{i=1}^{10} C_{ij}^{-1} p_i p_j + \sum_{j=1}^{2} \xi_j^2 \,, \tag{11.2}$$

where C^{-1} is the inverse of the correlation matrix of measurements x_i used in the fit.

We perform a 2D scan in the plane of variables a and δ_1. At each scan point (a and δ_1 are fixed), we perform a fit with two free parameters, $\xi_{\mathcal{R}_v}$ and $\xi_{\Delta m}$. The fit results for the best solution are shown in figure 11 and table 7. The χ^2 value is 9.0, which for 6 degrees of

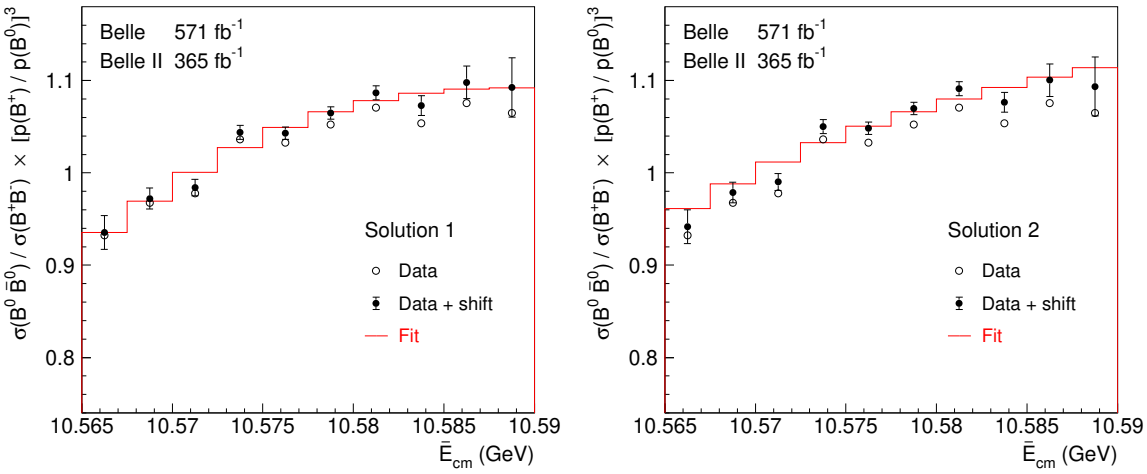

Figure 11: Energy dependence of the ratio of dressed $e^+e^- \to B^0\bar{B}^0$ and $e^+e^- \to B^+B^-$ cross sections divided by the phase-space factor $(p_{B^0}/p_{B^+})^3$. The black dots with error bars are the measured values shifted by the correlated systematic uncertainty (the second term in eq. (11.1)) according to the fit results; the open black circles are the measured values before the shift. The red histogram shows the result of the fit to the phenomenological model. The left and right panels show solutions 1 and 2, respectively.

Table 7: Parameters of two solutions in the (a, δ_1) plane.

	Solution 1	Solution 2
a, fm	1.062 ± 0.094	$0.24^{+0.24}_{-0.15}$
δ_1, rad	$0.218^{+0.076}_{-0.097}$	$-0.19^{+0.16}_{-0.33}$
$\xi_{\mathcal{R}_v}$	0.31 ± 0.03	0.53 ± 0.03
$\xi_{\Delta m}$	0.63 ± 0.27	0.49 ± 0.27

freedom corresponds to a p-value of 17%. The corresponding contours at the 1, 2, and 3 σ levels are shown in figure 12. The contours are determined from the changes in χ^2 of the fit relative to the optimal value. There is a second solution whose χ^2 value is worse by 8.6 units (figure 11 and table 7). The second solution corresponds to a small value of a, which is below the confinement scale. Such a small interaction range is theoretically disfavored.

The scattering phase δ_1 in solution 1 is positive at the level of about 2 σ. A positive scattering phase would correspond to an attractive isovector $B\bar{B}$ potential. In the limit of a large b-quark mass, the strong interaction potential is universal, i.e. the same for the

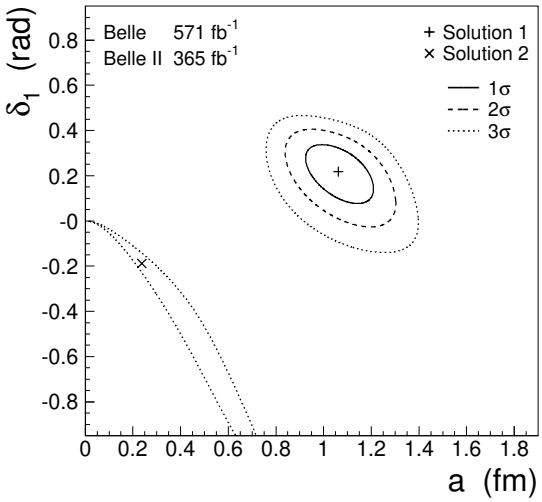

Figure 12: The (a, δ_1) plane. Here a and δ_1 are phenomenological parameters of an isovector $B\bar{B}$ potential described in the text.

$B\bar{B}$, $B\bar{B}^*$, and $B^*\bar{B}^*$ channels. Thus, our results are relevant for understanding molecular states with isospin one in all these channels, in particular $Z_b(10610)$ and $Z_b(10650)$ [37].

12 Conclusions

We measure the $m(B^0) - m(B^+)$ mass difference to be

$$\Delta m = (0.495 \pm 0.024 \pm 0.005)\,\mathrm{MeV}/c^2. \tag{12.1}$$

A key ingredient of this measurement is the determination of the energy dependence of the $\mathcal{R} = \sigma(e^+e^- \to B^0\bar{B}^0)/\sigma(e^+e^- \to B^+B^-)$ cross-section ratio that we constrain using the variation of the average e^+e^- c.m. energy over the data-taking periods of Belle and Belle II.

The result in eq. (12.1) is significantly different from a similar measurement by BaBar, $\Delta m = 0.33 \pm 0.05 \pm 0.03\,\mathrm{MeV}/c^2$ [7], which currently dominates the world average [8]. In contrast to the analysis reported here, in ref. [7] the energy dependence of $\mathcal{R}$ was not determined experimentally; instead, the phase-space hypothesis $\mathcal{R} = (p_{B^0}/p_{B^+})^3$ was assumed. If we use the phase space hypothesis in our combined fit, we obtain a value of Δm that is consistent with the BaBar measurement. However, the fit quality is very poor. In particular, the fit fails to describe the $\tilde{M}_{\mathrm{bc}}$ distributions of B^0 and B^+ candidates. We exclude the phase-space hypothesis at about the $10\,\sigma$ level. Using direct measurements of $m(B^0)$ and $m(B^+)$ [8], we obtain $\Delta m = (0.21 \pm 0.22)\,\mathrm{MeV}/c^2$, which is consistent with our measurement at the $1.3\,\sigma$ level.

We find that the combined fit is sensitive to $\mathcal{R}$ in a wider energy range than covered by the direct measurement, so we perform an additional study to measure the dependence $\mathcal{R}(E_{\mathrm{cm}})$. Here, $\mathcal{R}(E_{\mathrm{cm}})$ is treated as a binned distribution where the values in each bin are determined by a modified version of our combined fit. The resulting values are reported from the $B\bar{B}$ threshold up to 10.59 GeV. We also perform a phenomenological analysis

of the $\mathcal{R}(E_{\rm cm})$ results to determine the parameters of the isovector $B\bar{B}$ potential. At the $2\,\sigma$ level, we find an attractive isovector $B\bar{B}$ potential. Additional data closer to the $B\bar{B}$ threshold could help to improve the precision in $\mathcal{R}$ and in the phenomenological model parameters.

13 Acknowledgements

This work, based on data collected using the Belle II detector, which was built and commissioned prior to March 2019, and data collected using the Belle detector, which was operated until June 2010, was supported by Higher Education and Science Committee of the Republic of Armenia Grant No. 23LCG-1C011; Australian Research Council and Research Grants No. DP200101792, No. DP210101900, No. DP210102831, No. DE220100462, No. LE210100098, and No. LE230100085; Austrian Federal Ministry of Education, Science and Research, Austrian Science Fund (FWF) Grants DOI: 10.55776/P34529, DOI: 10.55776/J4731, DOI: 10.55776/J4625, DOI: 10.55776/M3153, and DOI: 10.55776/PAT1836324, and Horizon 2020 ERC Starting Grant No. 947006 "InterLeptons"; Natural Sciences and Engineering Research Council of Canada, Digital Research Alliance of Canada, and Canada Foundation for Innovation; National Key R&D Program of China under Contract No. 2024YFA1610503, and No. 2024YFA1610504 National Natural Science Foundation of China and Research Grants No. 11575017, No. 11761141009, No. 11705209, No. 11975076, No. 12135005, No. 12150004, No. 12161141008, No. 12405099, No. 12475093, and No. 12175041, and Shandong Provincial Natural Science Foundation Project ZR2022JQ02; the Czech Science Foundation Grant No. 22-18469S, Regional funds of EU/MEYS: OPJAK FORTE CZ.02.01.01/00/22_008/0004632 and Charles University Grant Agency project No. 246122; European Research Council, Seventh Framework PIEF-GA-2013-622527, Horizon 2020 ERC-Advanced Grants No. 267104 and No. 884719, Horizon 2020 ERC-Consolidator Grant No. 819127, Horizon 2020 Marie Sklodowska-Curie Grant Agreement No. 700525 "NIOBE" and No. 101026516, and Horizon 2020 Marie Sklodowska-Curie RISE project JENNIFER2 Grant Agreement No. 822070 (European grants); L'Institut National de Physique Nucléaire et de Physique des Particules (IN2P3) du CNRS and L'Agence Nationale de la Recherche (ANR) under Grant No. ANR-23-CE31-0018 (France); BMFTR, DFG, HGF, MPG, and AvH Foundation (Germany); Department of Atomic Energy under Project Identification No. RTI 4002, Department of Science and Technology, and UPES SEED funding programs No. UPES/R&D-SEED-INFRA/17052023/01 and No. UPES/R&D-SOE/20062022/06 (India); Israel Science Foundation Grant No. 2476/17, U.S.-Israel Binational Science Foundation Grant No. 2016113, and Israel Ministry of Science Grant No. 3-16543; Istituto Nazionale di Fisica Nucleare and the Research Grants BELLE2, and the ICSC – Centro Nazionale di Ricerca in High Performance Computing, Big Data and Quantum Computing, funded by European Union – NextGenerationEU; Japan Society for the Promotion of Science, Grant-in-Aid for Scientific Research Grants No. 16H03968, No. 16H03993, No. 16H06492, No. 16K05323, No. 17H01133, No. 17H05405, No. 18K03621, No. 18H03710, No. 18H05226, No. 19H00682, No. 20H05850, No. 20H05858, No. 22H00144, No. 22K14056, No. 22K21347, No. 23H05433, No. 26220706, and No. 26400255, and the Ministry of Education, Culture, Sports, Sci-

ence, and Technology (MEXT) of Japan; National Research Foundation (NRF) of Korea Grants No. 2021R1-F1A-1064008, No. 2022R1-A2C-1003993, No. 2022R1-A2C-1092335, No. RS-2016-NR017151, No. RS-2018-NR031074, No. RS-2021-NR060129, No. RS-2023-00208693, No. RS-2024-00354342 and No. RS-2025-02219521, Radiation Science Research Institute, Foreign Large-Size Research Facility Application Supporting project, the Global Science Experimental Data Hub Center, the Korea Institute of Science and Technology Information (K25L2M2C3) and KREONET/GLORIAD; Universiti Malaya RU grant, Akademi Sains Malaysia, and Ministry of Education Malaysia; Frontiers of Science Program Contracts No. FOINS-296, No. CB-221329, No. CB-236394, No. CB-254409, and No. CB-180023, and SEP-CINVESTAV Research Grant No. 237 (Mexico); the Polish Ministry of Science and Higher Education and the National Science Center; the Ministry of Science and Higher Education of the Russian Federation and the HSE University Basic Research Program, Moscow; University of Tabuk Research Grants No. S-0256-1438 and No. S-0280-1439 (Saudi Arabia), and Researchers Supporting Project number (RSPD2025R873), King Saud University, Riyadh, Saudi Arabia; Slovenian Research Agency and Research Grants No. J1-50010 and No. P1-0135; Ikerbasque, Basque Foundation for Science, State Agency for Research of the Spanish Ministry of Science and Innovation through Grant No. PID2022-136510NB-C33, Spain, Agencia Estatal de Investigacion, Spain Grant No. RYC2020-029875-I and Generalitat Valenciana, Spain Grant No. CIDEGENT/2018/020; the Swiss National Science Foundation; The Knut and Alice Wallenberg Foundation (Sweden), Contracts No. 2021.0174, No. 2021.0299, and No. 2023.0315; National Science and Technology Council, and Ministry of Education (Taiwan); Thailand Center of Excellence in Physics; TUBITAK ULAKBIM (Turkey); National Research Foundation of Ukraine, Project No. 2020.02/0257, and Ministry of Education and Science of Ukraine; the U.S. National Science Foundation and Research Grants No. PHY-1913789 and No. PHY-2111604, and the U.S. Department of Energy and Research Awards No. DE-AC06-76RLO1830, No. DE-SC0007983, No. DE-SC0009824, No. DE-SC0009973, No. DE-SC0010007, No. DE-SC0010073, No. DE-SC0010118, No. DE-SC0010504, No. DE-SC0011784, No. DE-SC0012704, No. DE-SC0019230, No. DE-SC0021274, No. DE-SC0021616, No. DE-SC0022350, No. DE-SC0023470; and the Vietnam Academy of Science and Technology (VAST) under Grants No. NVCC.05.02/25-25 and No. DL0000.05/26-27.

These acknowledgements are not to be interpreted as an endorsement of any statement made by any of our institutes, funding agencies, governments, or their representatives.

We thank the SuperKEKB team for delivering high-luminosity collisions; the KEK cryogenics group for the efficient operation of the detector solenoid magnet and IBBelle on site; the KEK Computer Research Center for on-site computing support; the NII for SINET6 network support; and the raw-data centers hosted by BNL, DESY, GridKa, IN2P3, INFN, PNNL/EMSL, and the University of Victoria.

References

[1] J. L. Goity and C. P. Jayalath, "Strong and Electromagnetic Mass Splittings in Heavy Mesons," Phys. Lett. B **650**, 22 (2007).

[2] S. Dubynskiy, A. Le Yaouanc, L. Oliver, J. C. Raynal and M. B. Voloshin, "Isospin breaking in the yield of heavy meson pairs in e^+e^- annihilation near threshold," Phys. Rev. D **75**, 113001 (2007).

[3] A. Bondar *et al.* [Belle Collaboration], "Observation of two charged bottomonium-like resonances in $\Upsilon(5S)$ decays," Phys. Rev. Lett. **108**, 122001 (2012).

[4] A. E. Bondar, A. I. Milstein, R. V. Mizuk, and S. G. Salnikov, "Effects of isospin violation in the $e^+e^- \to B^{(*)}\bar{B}^{(*)}$ cross sections," JHEP **05** (2022) 170.

[5] M. B. Voloshin, "Variation of the relative yield of charged and neutral B mesons across the $\Upsilon(4S)$ resonance," Mod. Phys. Lett. A **18**, 1783 (2003).

[6] M. B. Voloshin, "Relative yield of charged and neutral heavy meson pairs in e^+e^- annihilation near threshold," Phys. Atom. Nucl. **68**, 771 (2005).

[7] B. Aubert *et al.* [BaBar Collaboration], "Measurement of the Mass Difference $m(B^0) - m(B^+)$," Phys. Rev. D **78**, 011103 (2008).

[8] S. Navas *et al.* [Particle Data Group], "Review of particle physics," Phys. Rev. D **110**, 030001 (2024).

[9] R. Mizuk *et al.* [Belle Collaboration], "Measurement of the energy dependence of the $e^+e^- \to B\bar{B}$, $B\bar{B}^*$ and $B^*\bar{B}^*$ exclusive cross sections," JHEP **06** (2021) 137.

[10] I. Adachi *et al.* [Belle-II Collaboration], "Measurement of the energy dependence of the $e^+e^- \to B\bar{B}$, $B\bar{B}^*$, and $B^*\bar{B}^*$ cross sections at Belle II," JHEP **10** (2024) 114.

[11] B. Aubert *et al.* [BaBar Collaboration], "Measurement of the $e^+e^- \to b\bar{b}$ cross section between $\sqrt{s} = 10.54\,\mathrm{GeV}$ and $11.20\,\mathrm{GeV}$," Phys. Rev. Lett. **102**, 012001 (2009).

[12] A. Abashian *et al.* [Belle Collaboration], "The Belle Detector," Nucl. Instrum. Meth. A **479**, 117 (2002).

[13] J. Brodzicka *et al.* [Belle Collaboration], "Physics Achievements from the Belle Experiment," PTEP **2012**, 04D001 (2012).

[14] S. Kurokawa *et al.*, "Overview of the KEKB accelerators," Nucl. Instrum. Meth. A **499**, 1 (2003).

[15] T. Abe *et al.*, "Achievements of KEKB," PTEP **2013**, 03A001 (2013).

[16] Z. Natkaniec *et al.*, "Status of the Belle silicon vertex detector," Nucl. Instrum. Meth. A **560**, 1 (2006).

[17] T. Abe *et al.* [Belle II Collaboration], "Belle II Technical Design Report," [arXiv:1011.0352 [physics.ins-det]].

[18] E. Kou *et al.* [Belle II Collaboration], "The Belle II Physics Book," PTEP **2019**, 123C01 (2019) [erratum: PTEP **2020**, 029201 (2020)].

[19] K. Akai *et al.* [SuperKEKB], "SuperKEKB Collider," Nucl. Instrum. Meth. A **907**, 188 (2018).

[20] D. J. Lange, "The EvtGen particle decay simulation package," Nucl. Instrum. Meth. A **462**, 152 (2001).

[21] T. Sjostrand, S. Mrenna and P. Z. Skands, "PYTHIA 6.4 Physics and Manual," JHEP **05** (2006) 026.

[22] B. F. L. Ward, S. Jadach and Z. Wąs, "Precision calculation for $e^+e^- \to 2f$: The KK MC project," Nucl. Phys. B Proc. Suppl. **116**, 73 (2003).

[23] T. Sjöstrand, S. Ask, J. R. Christiansen, R. Corke, N. Desai, P. Ilten, S. Mrenna, S. Prestel, C. O. Rasmussen, and P. Z. Skands, "An introduction to PYTHIA 8.2," Comput. Phys. Commun. **191**, 159 (2015).

[24] R. Brun *et al.*, "GEANT: detector description and simulation tool; March 1994," CERN Program Library, CERN, Geneva, 1993. Long Writeup W5013.

[25] S. Agostinelli *et al.*, "GEANT4 – a simulation toolkit," Nucl. Instrum. Meth. A **506**, 250 (2003).

[26] T. Kuhr *et al.* [Belle II Framework Software Group], "The Belle II Core Software," Comput. Softw. Big Sci. **3**, 1 (2019).

[27] Belle II Collaboration, "Belle II Analysis Software Framework (basf2)," https://doi.org/10.5281/zenodo.5574115.

[28] M. Gelb *et al.*, "B2BII: Data Conversion from Belle to Belle II," Comput. Softw. Big Sci. **2**, 9 (2018).

[29] T. Keck *et al.*, "The Full Event Interpretation: An Exclusive Tagging Algorithm for the Belle II Experiment," Comput. Softw. Big Sci. **3**, 6 (2019).

[30] E.A. Kuraev and V.S. Fadin, "On Radiative Corrections to e^+e^- Single Photon Annihilation at High-Energy," Sov. J. Nucl. Phys. **41**, 466 (1985).

[31] R. Zlebcik, "The tracking and measurement of the beam-related parameters at Belle II," https://zenodo.org/records/8119739.

[32] S. Banerjee *et al.* [Heavy Flavor Averaging Group (HFLAV)], "Averages of b-hadron, c-hadron, and τ-lepton properties as of 2023," [arXiv:2411.18639 [hep-ex]].

[33] V. Zhukova *et al.* [Belle], "Measurement of the $e^+e^- \to B_s^0 \bar{B}_s^0 X$ cross section in the energy range from 10.63 to 11.02 GeV using inclusive D_s^+ and D^0 production," JHEP **08** (2023) 131.

[34] R. Aaij *et al.* [LHCb], "Observation of the resonant character of the $Z(4430)^-$ state," Phys. Rev. Lett. **112**, 222002 (2014).

[35] K. Chilikin *et al.* [Belle], "Observation of a new charged charmoniumlike state in $\bar{B}^0 \to J/\psi K^- \pi^+$ decays," Phys. Rev. D **90**, 112009 (2014).

[36] M. B. Voloshin, "Charged-to-neutral meson yield ratio at $\psi(3770)$ and $\Upsilon(4S)$ revisited," Phys. Rev. D **97**, 114023 (2018).

[37] A. E. Bondar, A. Garmash, A. I. Milstein, R. Mizuk and M. B. Voloshin, "Heavy quark spin structure in Z_b resonances," Phys. Rev. D **84**, 054010 (2011).

[38] Supplemental material is available at https://gitlab.desy.de/belle2/physics/quark/b2n-2024-029_dm/ (file xsecb_rat.tar.gz).

[39] L.D. Landau and E.M. Lifshitz, "Quantum Mechanics (Non-relativistic Theory)," Third Edition, Pergamon, Oxford, 1977.

A Energy dependence of $\sigma(e^+e^- \to b\bar{b})$ and $\mathcal{R}$

Figure 13 shows the fitted energy dependence of $[\sigma(e^+e^- \to B^0\bar{B}^0)+\sigma(e^+e^- \to B^+B^-)]/\sigma_0$ and $\mathcal{R} = \sigma(e^+e^- \to B^0\bar{B}^0)/\sigma(e^+e^- \to B^+B^-)$, where $\sigma(e^+e^- \to B^0\bar{B}^0)$ and $\sigma(e^+e^- \to B^+B^-)$ are the corresponding dressed cross sections, and $\sigma_0 = (4\pi\alpha/3)/E_{\rm cm}^2$ is the Born-level $e^+e^- \to \mu^+\mu^-$ cross section. In the panels of figure 13, we show the contribution

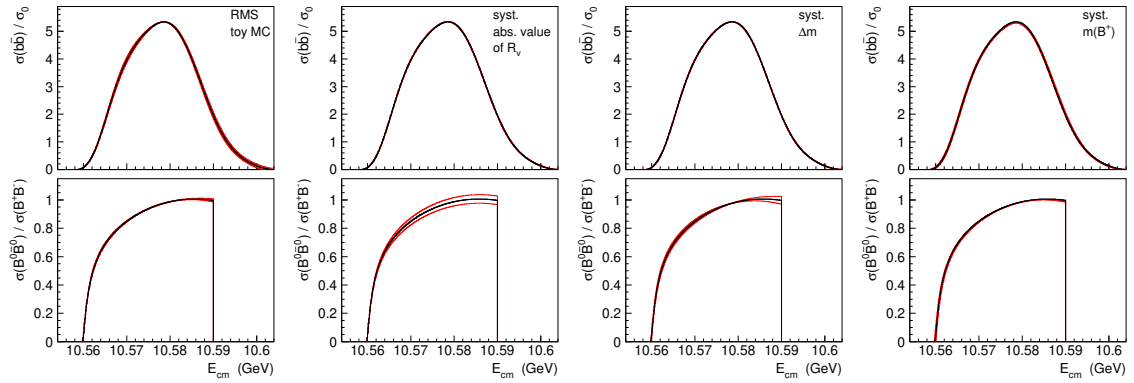

Figure 13: Energy dependence of (top) $[\sigma(e^+e^- \to B^0\bar{B}^0) + \sigma(e^+e^- \to B^+B^-)]/\sigma_0$ and (bottom) $\sigma(e^+e^- \to B^0\bar{B}^0)/\sigma(e^+e^- \to B^+B^-)$, where $\sigma(e^+e^- \to B^0\bar{B}^0)$ and $\sigma(e^+e^- \to B^+B^-)$ are the corresponding dressed cross sections, and $\sigma_0 = (4\pi\alpha/3)/E_{\rm cm}^2$ is the Born-level $e^+e^- \to \mu^+\mu^-$ cross section. The black curve in each plot is the result of the nominal fit. The red curves in the leftmost plots show the deviations corresponding to the RMS of the fit results for the pseudo-experiments. The remaining plots show deviations corresponding to the main sources of systematic uncertainty: uncertainties in $\mathcal{R}_{\rm v}$, Δm, and $m(B^+)$.

of statistical uncertainty estimated using pseudo-experiments and the main sources of systematic uncertainty. We fit pseudo-experiments fixing the Δm value and take into account the uncertainty in Δm as systematic uncertainty. The ratio $\mathcal{R}$ is shown only below $E_{\rm cm} = 10.59\,\text{GeV}$, since it is not constrained by our fit above this value.

These plots in numerical format are given in the supplemental material [38]. We present the values of the curves with a step in energy of 0.1 MeV. To provide information on statistical uncertainty, the material contains the fit results for 1000 pseudo-experiments.

B Phenomenological model

The energy dependence for the dressed cross-section ratio $\sigma(e^+e^- \to B^0\bar{B}^0)/\sigma(e^+e^- \to B^+B^-)$, arising from the mass difference $m(B^0) - m(B^+)$ and the electromagnetic interaction between B^+ and B^- for *point-like* B-mesons is given by the expression

$$\mathcal{R}_0 = \left(\frac{p_{B^0}}{p_{B^+}}\right)^3 \frac{1-\exp(-2\pi\lambda)}{2\pi\lambda}\,\frac{1}{1+\lambda^2}, \tag{B.1}$$

where $\lambda = \alpha/(2v_c)$ is the Coulomb parameter with v_c being the velocity of one charged B meson in the c.m. system [39].

The expression in eq. (B.1) does not take into account two effects: the finite size of the B mesons and the scattering phase in the isovector channel, which changes the relative phase between the outgoing $B^0\bar{B}^0$ and B^+B^- waves. These two effects were studied in ref. [2] for P-wave production, where both isospin breaking effects were treated as perturbations of the potential at linear order. The general formula in terms of the difference $\Delta V(r)$ of the potentials for the $B^0\bar{B}^0$ and B^+B^- pairs is

$$\mathcal{R} = 1 - \frac{1}{v}\,\mathrm{Im}\left[e^{2i\delta_1}\int_a^\infty e^{2ipr}\left(1+\frac{i}{pr}\right)^2\Delta V(r)\,dr\right]\,, \tag{B.2}$$

where v and p are the average B^0 and B^+ velocity and momentum, respectively.

The lower limit a in the integral in eq.(B.2) is a short-distance cutoff in the following sense. The difference in the potential ΔV can be defined as long as the individual channels $B^0\bar{B}^0$ and B^+B^- can be distinguished. However, at short distances where the mesons overlap due to their finite spatial size, the two channels are generally strongly mixed and thus cannot be distinguished. Thus any difference in the potential ΔV should vanish at short distances. This can be implemented by introducing [2] one effective cutoff distance a, so that $\Delta V = 0$ at $r < a$.

The potential difference due to the mass splitting and the Coulomb interaction has the form $\Delta V = 2\Delta m - \alpha/r$, and the integral in eq. (B.2) is given as [2]

$$\begin{aligned}
&\int_a^\infty e^{2ipr}\left(1+\frac{i}{pr}\right)^2\Delta V(r)\,dr = \\
&-\frac{\Delta m}{p}\left[\frac{2\,\cos 2\,pa}{pa}+\sin 2\,pa+i\left(\frac{2\sin 2\,pa}{pa}-\cos 2\,pa\right)\right] \\
&+\alpha\left[\frac{\cos 2pa}{2(pa)^2}+\frac{\sin 2pa}{pa}-\mathrm{Ci}(2pa)+i\left(\frac{\pi}{2}-\frac{\cos 2pa}{pa}+\frac{\sin 2pa}{2(pa)^2}-\mathrm{Si}(2pa)\right)\right]\,,
\end{aligned} \tag{B.3}$$

where $\mathrm{Si}(z)$ and $\mathrm{Ci}(z)$ are the integral sine and cosine functions.

For a quantitative comparison of the obtained expression for $\mathcal{R}$ with experiment, it is necessary to take into account the dependence of the scattering phase δ_1 on energy. The scattering phase in a wave with angular momentum ℓ is found from the formula [39]

$$\delta_1^{(\ell)} = -\frac{\pi M}{2}\int_0^\infty V_1(r)\left[J_{\ell+1/2}(pr)\right]^2 r\,dr\,, \tag{B.4}$$

where $J_\nu(z)$ is the standard Bessel function and we take $\ell = 1$. In the model [36], $V_1(r)$ is assumed to take a constant value V_1 in the region $r < a$ and zero outside. Therefore eq. (B.4) becomes

$$\delta_1 = -\frac{\pi M}{2}\,V_1\int_0^a\left[J_{3/2}(pr)\right]^2 r\,dr\,, \tag{B.5}$$